國 立 交 通 大 學

顯示科技研究所

碩士論文

利用漸變式矽過多氧化矽多層膜結構

製做高密度矽量子點薄膜於光伏元件之應用

High Density Si Quantum Dot Thin Films

Using a Gradient Si-Rich Oxide Multilayer Structure

For Photovoltaic Devices Application

研 究 生：黃品睿

指導教授：李柏璁 教授

中 華 民 國 101 年 8 月

利用漸變式矽過多氧化矽多層膜結構
製做高密度矽量子點薄膜於光伏元件之應用

High Density Si Quantum Dot Thin Films
Using a Gradient Si-Rich Oxide Multilayer Structure
For Photovoltaic Devices Application

研 究 生：黃品睿　　Student：Pin-Ruei Huang

指導教授：李柏璁　博士　Advisor：Dr. Po-Tsung Lee

國 立 交 通 大 學

顯示科技研究所

碩 士 論 文

A Thesis

Submitted to Department of Photonic and Display Institute

College of Electrical Engineering and Computer Science

National Chiao Tung University

In partial Fulfillment of the Requirements

for the Degree of Master

in

Electro-Optical Engineering

August 2012

Hsinchu, Taiwan, Republic of China

中華民國 101 年 8 月

利用漸變式矽過多氧化矽多層膜結構
製做高密度矽量子點薄膜於光伏元件之應用

研究生：黃品睿

指導教授：李柏璁 博士

國立交通大學顯示科技研究所

摘 要

矽基太陽能電池是目前全球市佔率最高的太陽能電池種類，加上其原料充足與製程技術成熟等優勢，未來前景仍相當被看好；為了更進一步提升元件效率與降低製程成本以達到第三代太陽能電池的目標，全矽基多接面太陽能電池正被廣泛地研究與開發。而其中具奈米結晶態的矽量子點薄膜則被視為極具潛力能克服矽基材料的能隙限制，以解決短波長光子的嚴重損耗議題。

截至目前，國際上的研究團隊製做的矽量子點薄膜以矽過多氧化矽(silicon-rich oxide)單層膜或二氧化矽(silicon dioxide)/矽過多氧化矽(silicon-rich oxide)多層膜結構為主，但前者不易調控量子點尺寸，後者則有量子點間距過大的問題，加上兩者皆無法達到高密度的矽量子點形成，導致元件的光激載子傳輸嚴重受限，整體效率仍有待改善。

故本篇論文提出以漸變式矽氧濃度之氧化矽薄膜取代二氧化矽侷限層的構想，藉由在沉積時連續性調控矽氧組成比，使其每一週期的矽濃度呈現漸變式分佈(低→高→低)，以此漸變濃度結構輔助後續退火過程中的奈米結晶矽形成，期望能同時達到矽量子點的尺寸調控及間距縮短，大幅改善光激載子傳輸效益，以提升矽量子點型太陽能電池之工作效率。

High Density Si Quantum Dot Thin Films Using a Gradient Si-Rich Oxide Multilayer Structure For Photovoltaic Devices Application

Student: Pin-Ruei Huang
Advisor: Dr. Po-Tsung Lee

Display Institute
National Chiao Tung University

Abstract

So far, the Si-based solar cell is the highest global market share and the good development potential due to the plentiful materials and the well-developed fabrication technique. In order to achieve the goal of the third generation solar cells with high efficiency and low cost, all Si-based multiple-junction solar cell is widely investigated and developed nowadays. The nano-crystalline Si quantum dot (QD) thin film is one of the potential structures to overcome the bandgap limitation of Si-based materials.

Silicon-rich oxide (SRO) single layer and [SRO/SiO_2] multilayer (ML) thin films are the most commonly used deposition structures for Si QD thin films. However, the former is hard to control the QD's size and density simultaneously, the latter exists the QD's separation limitation due to the SiO_2 barrier layers inserted. Furthermore, the QD's density of both structures is still not high enough for a better PV application. These result in the difficulty for good photo-generated carrier's transportation and high conversion efficiency. Hence, to efficiently improve the carrier's transportation properties is a critical issue for the high efficiency Si-based solar cells integrating Si QD thin film.

In this study, we propose a more potential deposition structure by a gradient Si-rich oxide multilayer (GSRO-ML) structure for the QD size control and the high QD density. The nano-structure, crystalline, and optical properties of Si QD thin films using a GSRO-ML structure had been studied. It also shows the better photovoltaic properties than that using a [SRO/SiO_2]-ML structure. A higher conversion efficiency of Si QD thin films utilizing a GSRO-ML structure can be highly expected by using a heavy doping concentration in the near future.

Acknowledgements

碩士班生活到了尾聲，一千多個日子隨著每天每天的實驗飛快的流逝，回首這三個寒暑的學習以及歷練讓我成長了許多。這一路上感謝很多人的照顧，首先要感謝的是我的指導教授—**李柏璁老師**，提供給我們完好的研究環境以及豐富的實驗室資源，並在研究上適時的給予寶貴的意見。還有我最最敬愛的老大—**光揚學長**，抱歉很常惹你生氣，謝謝你的耐心指導以及包容我的白目和遲鈍，我想我唯一的優點應該就是使命必達吧。

還要感謝**贊博、岳哥、狗勾、佐哥、佳裕、胖胖、G 隆、yoyo 哥、小源**，不管是實驗上的討論還是生活瑣事，暢快的談天說地總是可以讓我忘掉實驗的疲憊；還有一起奮鬥的 98 同學們**小邱邱、金剛、崴崴學長、文齡、呂紹平、邱哥**，在那些日子，一起修課，一起做實驗，一起夜唱到天亮然後隔天繼續上課的爆肝生活我好懷念。雖然你們先走一步，但是我才不會忘記你們呢！以及一起打拚的 99 學弟們**小智、嶢嶢、權政**，尤其”感謝”權政，因為你總讓我”事倍功半”!加油!你們也快要可以寫誌謝了!還有 100 學弟**酷哥**和**小朱**，感謝你們平常總是幫我們跑腿處理一些瑣事，還有戲弄你們兩位真是我歡樂的來源，讓我忘了做實驗的辛苦。真的非常感謝實驗室的大家，每天生活在一起，不管是研究、運動、休閒總是有大家的記憶，謝謝你們，對我而言你們不只是學長/同學/學弟，也是家人。

另外要感謝冉老師實驗室的**治寬、良豪、小胖學弟**，對不起每次換 round 的時候都 delay，但你們從來沒有抱怨過我。還要感謝余老師實驗室的**劉孝威**，百忙之中還抽空幫我量效率，而且連一頓麥當當都不願意讓我請，都沒機會報答你。還有感謝**爐管帥哥**，謝謝你，讓我曾經有一年的時光，在登入奈中的時候都是帶著期待又愉悅的心情。最後，感謝你，因為有你才能讓我更有動力，我會一直努力朝你所在的地方前進.....。

最重要的，感謝老媽和老哥，我很少回家，應該是個不孝女無誤，不過感謝有你們，讓我可以無後顧之憂的專心在研究上。

過幾天，我即將邁入人生下一個階段—博士班研究生涯，所以這份誌謝……

.....to be continued

黃品睿 2012 年 9 月

于國立交通大學 401 室

Content

List of Figures

Chapter 1

Chapter 2

Chapter 3

Chapter 4

Chapter 5

List of Tables

Chapter 1

Chapter 4

Chapter 1 Introduction

1.1 Background

Energy, environment, and economy are the three major problems that plagued the development of modern society. The consumption of resource becomes larger with the development of industrialization and the population increasing, so it can be predicted the occurrence of energy crisis. Besides, the increase on average temperature of the earth and the acid rain due to the green house effect resulted from arising emission of green house gases(like CO_2 and SO_2, etc. …) emission after burning fossil fuel are two main issues of the environmental protection.

The problems mentioned above lead us to find out the best substitute energies, which are renewable and pollution-free such as wind, tides, geothermal heat and solar. Among them, solar energy is vital in the present times considering the fact that the power demand in the world is a never ending process. It’s promising to use solar energy to replace fossil fuel completely in the future with advanced technologies.

1.2 Solar Cell

The first solar cell (SC) was developed at Bell laboratories in 1883 by Charles Fritts who coated the semiconductor selenium with an extremely thin layer of gold to form the junctions. However, the conversion efficiency (~1%) was too low to be applied. It had not drawn attention until the oil crisis broke out in following decades. Recently, there are more and more researchers involving in efficiency enhancement. Fig. 1-1[1-1] is a timeline of the silicon solar cell's steady rise in efficiency. But for applications, not only efficiencies but also the cost of manufacturing are to be considered. According to the efficiency as a function of cost, solar cells can be classified into three generations as shown in Fig. 1-2 [1-2].

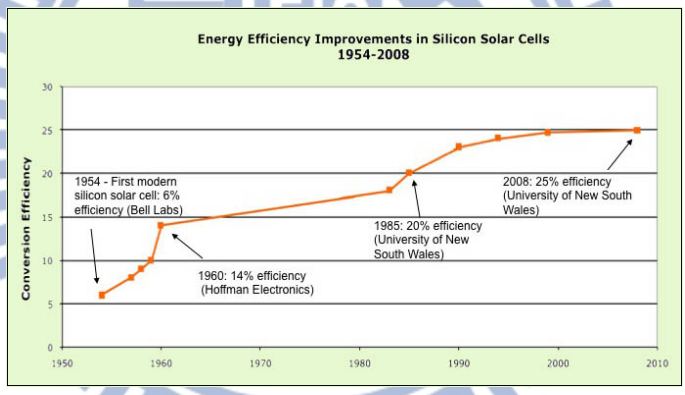

Fig. 1-1 Conversion efficiency improvements in silicon solar cells (1954-2008)[1-1].

The first generation SCs are silicon wafer-based SCs which are the most commonly used and well-developed ones. Although the SCs have high efficiencies, the production cost also high. In order to reduce the cost, the second generation SCs, such as amorphous silicon (a-Si) thin film SC, organic cells, and dye-sensitized SCs (DSSCs) are developed. The cost is quiet cheaper than that of the first generation SCs. On the other hand, the efficiency of the second generation SCs are lower than that of first generation SCs. Other main features of the second generation SCs are their flexibility and light-weight which make lots of application innovations

such as flexible solar panels. For achieving SCs with high efficiency which is potential to be larger than efficiency limit of SC with single bandgap (31%) and low producing cost, the third generation SCs are proposed like poly-Si SCs and nanocrystalline Si (NC-Si) SCs, etc. The strategies are abundant, non-toxic and durable, so the technologies can develop without pollutions. Even if the third generation SC is superior to the others, they are still in the research phase.

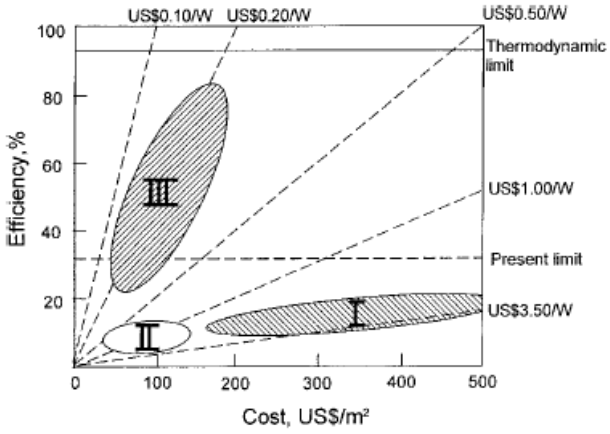

Fig. 1-2 Efficiency and cost projections for first-, second- and third-generation photovoltaic technology (wafers, thin-films, and advanced thin-films, respectively) [1-2].

1.3 Silicon Based Tandem Solar Cells

1.3.1 Energy Loss paths in Single Junction Solar Cells

There are five energy loss paths in standard single junction solar cells, including junction loss, contact loss, recombination loss, high-energy photon loss (also called thermalization loss) and low-energy photon loss (also called non-absorption loss) as shown in Fig. 1-3[1-3].

Thermalization loss occurs when the incident energy is larger than the bandgap, and non-absorption loss occurs when the incident energy is less than the bandgap. These two losses are the two most important losses in single-junction photovoltaic cells. In order to overcome the losses mentioned above, there are some approaches like: (a) increasing the number of bandgap for photon absorption from a wide-range spectrum; (b) capturing carrier before they thermalize to bandgap; (c) multiple carrier pair generation per high energy photon or single carrier pair generation with multiple low energy photons. Tandem solar cell, stacking sub-cells from large to small bandgap in turn, is a much more promising structure to achieve a high efficiency SC. NC-Si can be made very small size, less than 7 nm in diameter, and they behave like quantum dots (QDs), e.g. bandgap control with nanocrystal size, very fast optical transition, and multiple carrier, generation, owing to the three-dimensional quantum confinement of carrier [1-4]. NC-Si embedded in dielectric material cascaded with silicon-based solar cells is one of the proposed solar cell structures to achieve super high conversion efficiency due to its ability in energy bandgap engineering.

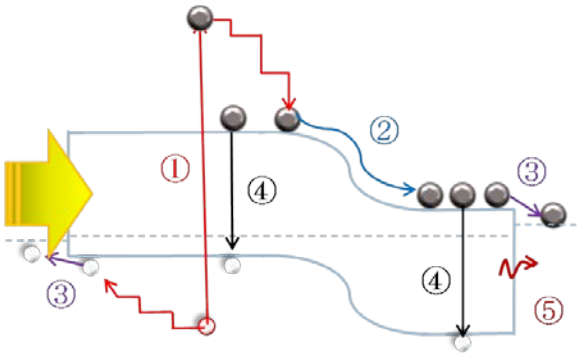

Fig. 1-3 Energy loss paths in a single junction solar cell: (1) high-energy photon loss, (2) junction loss, (3) contact loss, (4) recombination loss, (5) low-energy photon loss.

1.3.2 Quantum Confinement Effect

Behavior of particle waves confined in an infinite quantum well can be explained by three-dimensional (3-D) time-dependence Schrödinger's equation expressed as

$$-\frac{\hbar}{2m}\nabla^2\Psi\left(\vec{r}\right)+V\left(r\right)\Psi\left(\vec{r}\right)=E\Psi\left(\vec{r}\right) \tag{1-1}$$

We can obtain that allowance energy states are discrete and they depend on the width of the quantum well. The phenomenon comes from the quantum confinement effect. For particle-waves confined in nanoparticles covered in materials with finite barrier height, similar energy states can be obtained, as expressed by Eq. (1-2)

$$E_n=\frac{\hbar^2\pi^2}{2ma^2}n^2,\ \ n^2=\left(n_x^2+n_y^2+n_z^2\right) \tag{1-2}$$

where n_x, n_y, n_z are integers and equal to 1 for the ground state square box.

Discrete energy levels depend on the dimension of nanoparticles and barrier height between nanoparticles and materials which cover around them. Fig. 1-4 [1-5] shows the wave functions of different nanoparticles sizes with a fixed barrier height and those of different barrier with a fixed nanoparticle size. As a result, we can control effective E_g by tuning the QD's size and changing the matrix material.

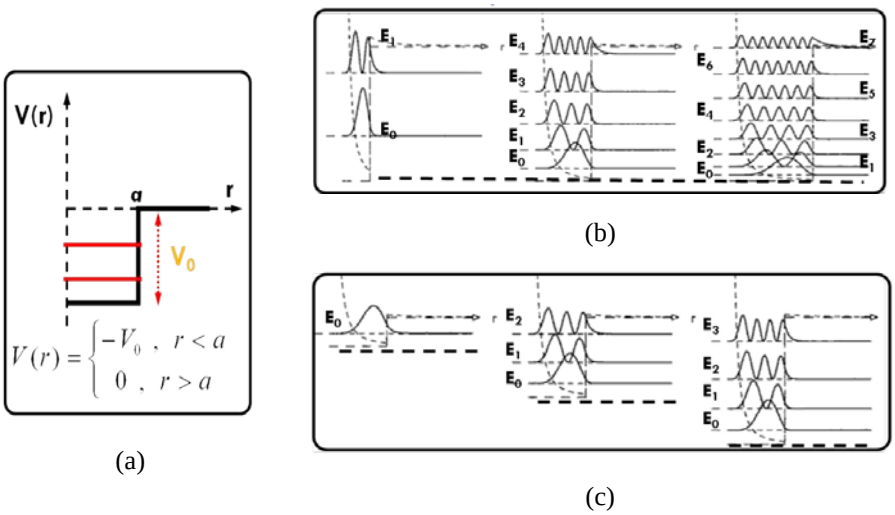

Fig. 1-4 Illustration of 3-D time-independence Schrödinger's equation and boundary conditions [1-5].

1.3.3 Tandem Solar Cell Using Si Quantum Dot Thin Films

From quantum theory, we know, when the QD's size is reduced to a few nanometers, the quantum confinement effect will occur. It will relax the K-space conservation requirement and transform the Si bandgap properties from indirect to quasi-direct and modify the effective E_g of Si. Fig. 1-5(a) shows that embedding Si QD in a wide bandgap material can lead to a highly –tunable effective bandgap. In addition, Fig. 1-5(b) shows that the effective E_g of Si QD can be widely modified by tuning the QD's size in SiO_2 or Si_3N_4 matrix material, and a larger bandgap than c-Si or a-Si material is also feasible using Si QD [1-6]. Therefore, we can integrate Si QD into Si-based SCs to reduce energy losses from mismatch bandgap.

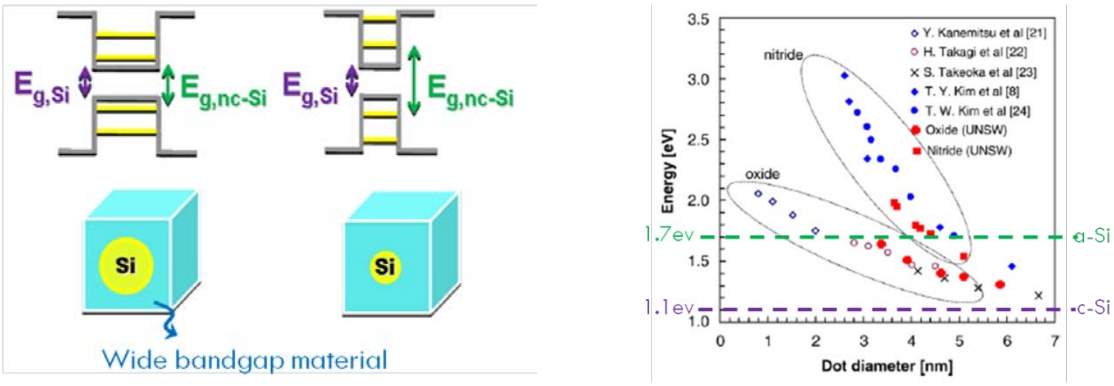

(a) (b)

Fig. 1-5 (a) Illustration of Si QD embedded in materials with different QD size. (b) Experimental bandgaps of Si QDs embedded in SiO_2 and SiN_x from other groups [1-6].

In order to achieve high efficiency and low cost solar cell, the third generation solar cells have been studied. One of the promising candidates is the tandem solar cell using Si QD thin films as shown in Fig. 1-6 [1-7]. The concept of the tandem solar cell is stacking different E_g of solar cells from large to small ones for the absorbing different energy of photons. The uppermost cell has the highest bandgap and lets the photon less than its bandgap passing through to lower bandgap cells underneath.

Tandem solar cells using Si QD thin films stacking materials with different energy bandgaps can utilize the wide solar spectrum more effectively. Table 1-1 [1-8] shows the best bandgap combinations under different numbers and their theoretical efficiencies.

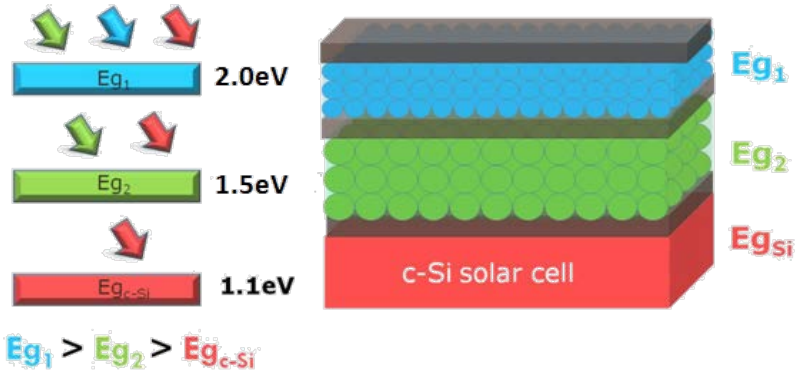

Fig. 1-6 Scheme of Si-based tandem solar cell [1-7].

Table 1-1 Theoretical efficiencies and corresponding band gap combination depending on the active cell layers [1-8].

Cell no.	Band gap energy combination (eV)	Efficiency
1	1.34	33.54
2	1.60/0.94	45.32
3	1.90/1.36/0.94	51.32
4	1.98/1.46/1.05/0.70	54.70
5	2.12/1.64/1.27/0.99/0.7	57.19

1.4 Paper Review

Si QD embedded in dielectric mediums have been investigated due to the potential for optoelectronic applications such as photovoltaic devices. Si QD thin films fabrication by various deposition techniques is preferable because of the greater potential of integration into conventional devices. Si QD precipitating from silicon-rich layers is one of fabrications of Si QD systems by means of vacuum deposition techniques. For Si precipitation from an Si-rich oxide layer, high temperature annealing of excess Si in an inert atmosphere is necessary to form Si QD with a few nanometers in diameter, for example, Si QD precipitation in oxide [1-2, 1-9, 1-10], nitride [1-11], and carbide [1-12, 1-13]. Eq. (1-3) describes this Si precipitation mechanism:

$$\mathrm{Si(O,N,C)_x} \rightarrow \left(\frac{1}{2}\right)\mathrm{Si}\left(\mathrm{O_2},\mathrm{N_{3/4}},\mathrm{C}\right) + \left(1-\frac{1}{2}\right)\mathrm{Si} \qquad (1\text{-}3)$$

1.4.1 Si-Rich-Oxide Single Layer (SRO-SL) Thin Film

Si QDs have been synthesized by several techniques such as microwave-induced or laser-induced decomposition of silane (SiH_4)-like precursors [1-14, 1-15], ion implantation of Si^+ [1-16, 1-17], electrochemical etching of Si wafers [1-18], low pressure chemical vapor deposition [1-19], plasma-enhanced chemical vapor deposition (PECVD) [1-20, 1-21], pulsed-laser deposition (PLD) of Si [1-22], and sputtering systems [1-8~1-12, 1-22]. In 2004, G.A. Kachurin et al. fabricated Si QD embedded in SiO_2 matrix by implantation of Si ions at a fluence of 10^{17} cm^{-2} in thermally SiO_2 layers and by subsequent annealing at 1000 or 1100°C for 2 h. Then P ions were implanted in the layers within the dose range of 10^{13}–10^{16} cm^{-2} [1-17]. In 2002, A. A. Gonza´lez-Ferna´ndez et al.[1-21] fabricated Si QDs embedded in SiO_2 matrix by PECVD with SiH_4 and N_2O as reactant gas sources. The silicon excess of the layers was controlled by modulating the ratio of the partial pressures produced by the precursor gases in the chamber ($P_{[N_2O]}/P_{[SiH_4]}$). After

deposition, all the PECVD samples were annealed in N_2 atmosphere at 1250°C for 60 min to induce Si nucleation and the formation of Si QD. In 2010, Mota-Pineda et al. [1-23] proposed the SiO_x/Si QDs heterolayers which were fabricated employing a radio frequency (RF) magnetron sputtering system. In this study, the SRO thin films are deposited by sputtering the Si target under different oxygen pressures; the nucleation of as-grown crystals is promoted by the rough topography of the oxide films acting as a template.

1.4.2 [SRO/SiO_2] Multilayer (ML) Thin Film

In order to obtain a narrow size distribution and more accurate size control, M. Zacharias et al. proposed the SiO/SiO_2 superlattices in 2002 [1-24]. Superlattices have been known since 1970, and they can be manufactured with the epitaxial growth techniques available to III-V compound semiconductor technology [1-25]. In their study, amorphous SiO_x/SiO_2 superlattices were prepared by reactive evaporation of SiO powders in oxygen atmosphere. After deposition the samples were annealed at 1100 °C for 1 hour under N_2 atmosphere to obtain the Si QDs. Phase separation and thermal crystallization of SiO/SiO_2 superlattices results in ordered arranged Si QDs. This deposition structure can promise the QD size control and the QD density by tuning the stoichiometry of SRO layers. Besides, in 2009, X. J. Hao et al. [1-26~ 1-28] made their Si QD thin films by sputtering. First, multiple alternative layers of amorphous SRO (SiO_x, $x<2$), and stoichiometric SiO_2 as precursor thin films were deposited by cosputtering with SiO_2 and Si targets and sputtering with single SiO_2. Then Si QDs were obtained after annealing at 1100°C for 1hr under N_2 atmosphere. The dimension and density of Si QD can be controlled by adjusting the thickness or Si content of amorphous SRO layer.

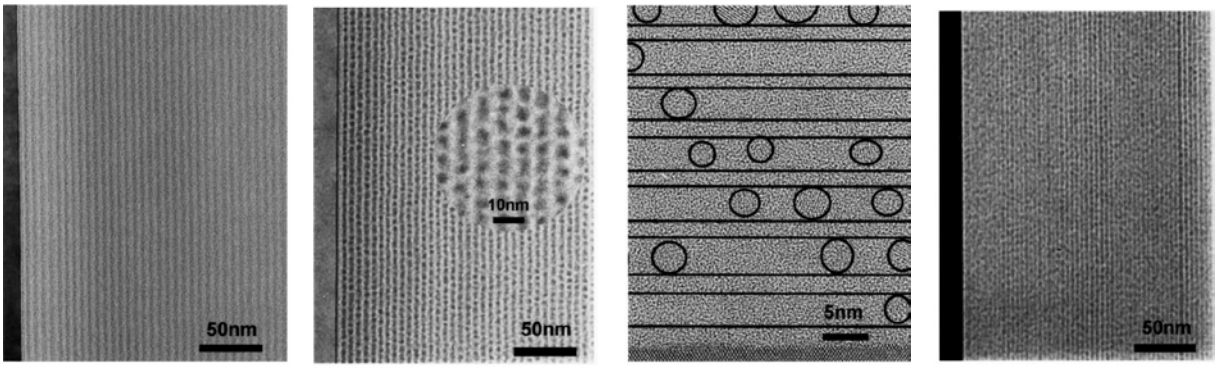

(a) (b) (c) (d)

Fig. 1- 7 Cross-sectional TEM images of SiO/SiO_2 superlattices: (a) As-prepared SiO/SiO_2 superlattice. The darker layers represent the SiO sublayers. (b) The same film after annealing. The separation of the nanocrystals by a thin oxide shell is clearly visible. (c) High resolution TEM image of the film. For clarity, the visible nanocrystals are highlighted by circles. The crystals are only found in the former SiO layers, which are emphasized by the lines in the image. (d) TEM image of a film with even thinner SiO layers ~2 nm after annealing [1-24].

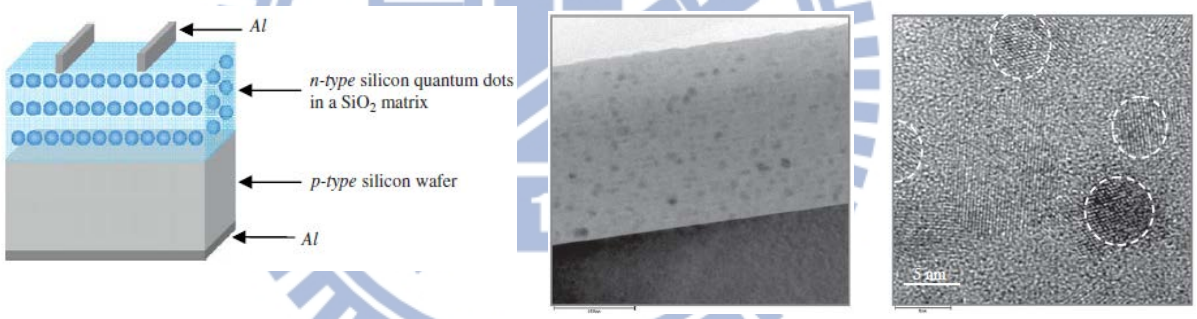

(a) (b) (c)

Fig. 1-8 (a) Schematic diagram of (n-type) Si QDs and (p-type) c-Si heterojunction solar cell. And transmission electron microscopy (TEM) images of Si quantum dots in SiO_2 matrix with (b) low-magnification and (c) high-resolution lattice images for 5 nm Si QDs.

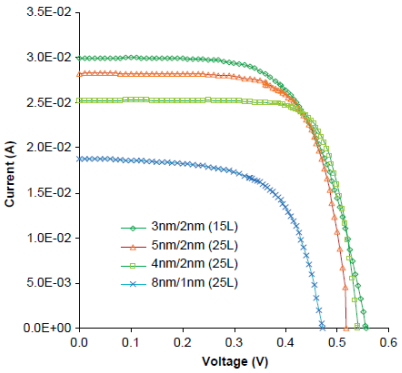

Fig. 1-9 Four different I–V characteristics of the (n-type) Si QDs/ (p-type) c-Si heterojunction devices.

Table 1-2 One-sun illuminated cell parameters of four different (n-type) Si QDs/ (p-type) c-Si heteroface devices measured at 298 K.

SRO/SiO_2 thickness (nm), number of bilayers	V_{oc} (mV)	J_{sc} (mA/cm^2)	FF (%)	Eff. (%)
3/2, 15 BL	556	29.8	63.83	10.58
4/2, 15 BL	540.3	25.0	76.8	10.4
5/2, 25 BL	517.9	27.9	72.3	10.5
8/1, 25 BL	470.8	18.6	65.1	5.7

One of important applications of Si QD thin films is photovoltaic devices. In 2009, S. Park et al. demonstrated that the efficiency of solar cells using Si QDs embedded in SiO_2 matrix (shown as Fig. 1-8) is up to 10.58 %[1-29]. In addition, in 2011, S. H. Hong et al.[1-30] proposed that active doping of boron atoms in nanometer silicon layers confined in a SiO_2 matrix. In their study, they demonstrated a p-type Si quantum dot (QD) solar cell with a high energy conversion efficiency (η) of 13.4 % was realized from a [B-doped $SiO_{1.0}$(2 nm)/SiO_2(2 nm)]$_{25}$ superlattices film with a B doping concentration of 4.0×10^{20} atoms cm^{-3}.

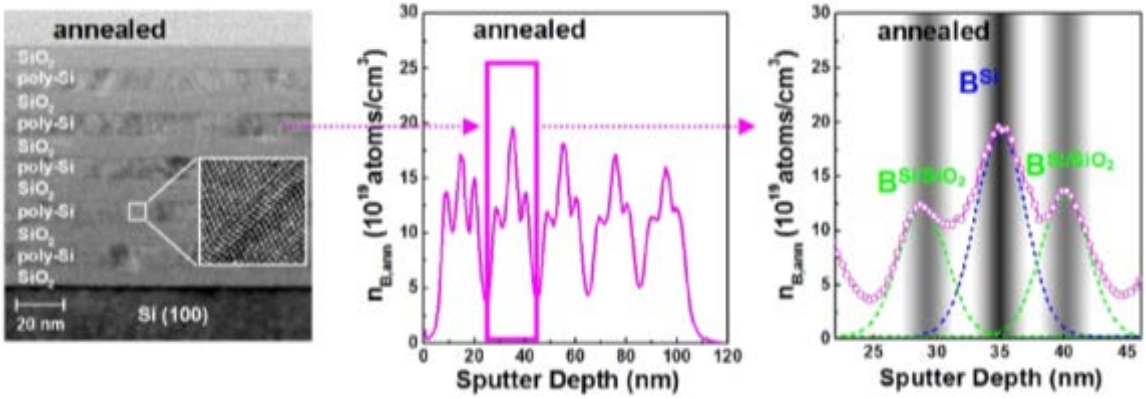

(a) (b) (c)

Fig. 1-10 (a) TEM images and (b) SIMS depth profiles of [SiO_2 (8 nm)/B-doped Si(10 nm)]$_5$ ML film with a B doping level of 1.7×10^{20} atoms cm^{-3} after annealing at 1100°C for 20 min by rapid thermal annealing.

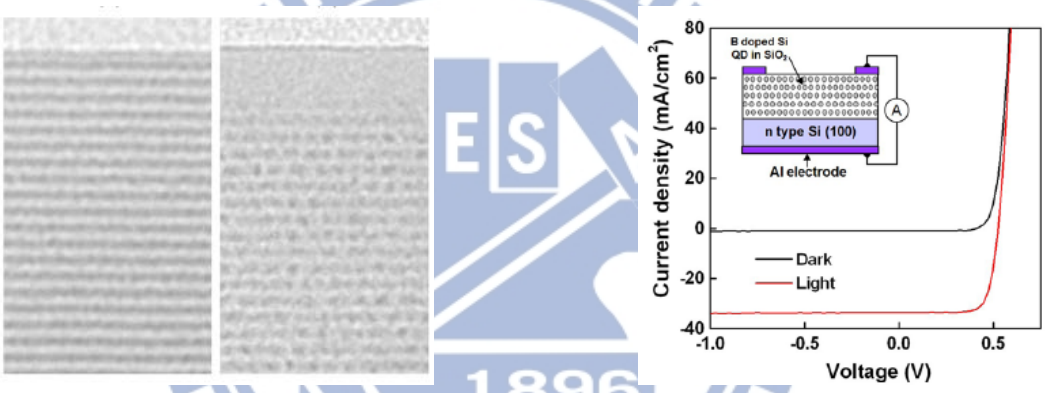

(a) (b)

Fig. 1-11 Representative TEM micrographs of the (a) as-deposited and (b) annealed [B-doped $SiO_{1.0}/SiO_2]_{25}$ superlattice films at 1100 ◦C for 10 min.

Fig. 1-12 Current–voltage (I-V) characteristics of a p-Si QDs/n-Si heterojunction solar cell under air mass 1.5 (AM 1.5G) illumination of 100 mW cm^{-2}.

In 2009, the all Si QD thin film solar cell has been fabricated on a quartz substrate by I. Perez-Wurfl et al. [1-31]. Though the P- and B-doping concentrations are heavy, the dark and illuminated I-V properties of this device are lower than Si QD thin film on Si wafer. The worse electrical properties may result from the barrier is low compared to a Schottky junction on bulk Si, and it is not assigned to a discontinuity in the conduction band but rather represents the

barrier that the electrons need to overcome to get injected into the depletion region located in the p-type side. On the other hand, it may result from the wide separation between QDs so that carriers can't transport smoothly.

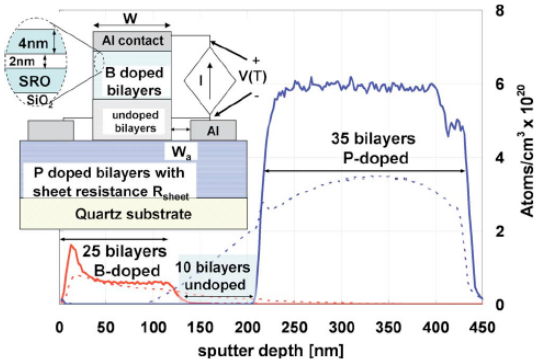

Fig. 1-13 SIMS data of as-deposited (solid line) and annealed (dotted line) p-i-n structure. Significant interdiffusion is observed after annealing for 1 hour at 1100 °C.

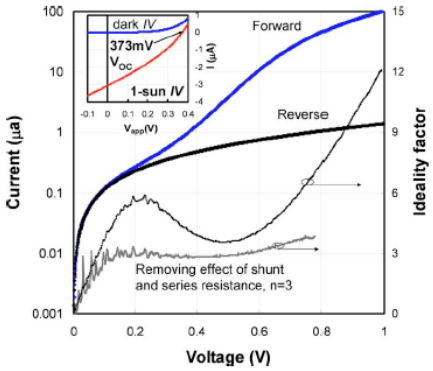

Fig. 1-14 Dark I-V characteristics of a 0.12 cm^2 diode. Inset shows the I-V characteristics under 1-sun illumination with V_{OC}=373 mV.

1.5 Motivation

The efficiency of Si-QD solar cell is still not high enough because there are still many problems exist in the SL and ML structure. For SRO-SL, it can't obtain the uniform QD's size and high QD's density simultaneously. For ML structure, such as the thickness of barrier layer (if barrier is too thin, it will lose the ability of confinement), interfacial defects at Si QD/SiO_2 matrix, built-in electrical field [1-26~ 1-28], etc. still need to settle.

In this study, we propose the gradient Si/O concentration ML (GSRO-ML) structure. After annealing, Si QDs will precipitate at the high Si/O region within a period layer. We expect that, in this structure, the separation between QDs will be reduced and the density of QDs will be increased but not influence the ability of size control. On the other hand, we adopt the highly phosphorus doping Si target and expect the increased conductivity will improve the electrical properties. We will discuss the characteristics about structural, crystalline, optical and electrical properties in this thesis.

Reference

[1-1] B. Chameides," Statistically Speaking: The Evolution of the Silicon Solar Cell," 2008

[1-2] M. A. Green, "Third Generation Photovoltaics: Ultra-high Conversion Efficiency at Low Cost," Prog. Photovolt: Res. Appl., 9, 123-135, 2001

[1-3] G. Conibeer , M. A. Green , R. Corkish , Y. Cho , E. C. Cho, C. W. Jiang, T. Fangsuwannarak, E. Pink, Y. Huang, T. Puzzer, T. Trupke, B. Richards, A. Shalav, K. L. Lin, "Silicon Nanostructures for Third Generation Photovoltaic Solar Cells," Thin Solid Films, 511 – 512, 654 – 662, 2006

[1-4] Y. Kanemitsu, T. Ogawa, K. Shiraishi, and K. Takeda, "Visible PL from Oxidized Si Nanometer-Sized Spheres: Exciton Confinement on A Spherical Shell," Phys. Rev. B, vol. 48, pp. 4883- 4886, 1993

[1-5] B. H. Bransden and C. J. Joachain, "Introduction to Quantum Mechanics, 2nd edition," 2000

[1-6] G. Conibeer, M. A. Green, E.C. Cho, D. Konig, Y. H. Cho, T. Fangsuwannarak, G. Scardera, E. Pink, Y. Huang, T. Puzzer, S. Huang, D. Song, C. Flynn, S. Park, X. Hao, and D. Mansfield," ," Thin Solid Film, 516, 6748-6756, 2008.

[1-7] M. A. Green, G. Conibeer, D. Konig, E.C. Cho, D. Song, Y. Cho, T. Fangsuwannarak, Y. Huang, G. Scardera, E. Pink, S. Huang, C. Jiang, T. Trupke, R. Corkish, T. Puzzer, "Progress with All Silicon Tandem Cells Based on Silicon Quantum Dots in A Dielectric Matrix." Proceedings 21st EU PVSEC, Dresden, 2006

[1-8] C. Feser, J. Lacombe, K. V. Maydell and C. Agert," A Simulation Study Towards A New Concept for Realization of Thin Film Triple Junction Solar Cells Based on Group IV Elements," Prog. Photovolt: Res. Appl., 20, 1, 74-81, 2011

[1-9] E. C. Cho, Y. H. Cho, T. Trupke, R. Corkish, G. Conibeer, and M. A. Green, "Silicon Nanostructures for All-Silicon Tandem Solar Cells," in Proceedings of the 19th European Photovoltaic Solar Energy Conference and Exhibition, 235, Paris, France, 2004.

[1-10] S. Lombardo and S. U. Campisano, "Electrical And Optical Properties of Semi-insulating Polycrystalline Silicon Thin Films: The Role of Microstructure And Doping," Materials Science and Engineering, 17, 8, 281–336, 1996.

[1-11] Y. Cho, E. C. Cho, Y. Huang, T. Trupke, G. Conibeer, and M. A. Green, "Silicon Quantum Dots In SiN_x Matrix for Third Generation Photovoltaics," in Proceedings of the 20th European Photovoltaic Solar Energy Conference and Exhibition, p. 47, Barcelona, Spain, June 2005

[1-12] Y. Kurokawa, S. Miyajima, A. Yamada, and M. Konagai, “Preparation of Nanocrystalline Silicon in Amorphous Silicon Carbide Matrix,” Japanese Journal of Applied Physics, 45, 40, L1064–L1066, 2006.

[1-13] D. Song, E. C. Cho, Y. H. Cho, G. Conibeer, Y. Huang, S. Huang, M. A. Green, “Evolution of Si (and SiC) nanocrystal precipitation in SiC matrix,” Thin Solid Films, 516, 12, 30, 3824–3830, 2008

[1-14] H. Takagi, H. Ogawa, Y. Yamazaki, A. Ishizaki, and T. Nakagiri,” Quantum Size Effects on Photoluminescence in Ultrafine Si Particles,” Appl. Phys. Lett. 56, 2379, 1990

[1-15] M. Ehbrecht, H. Ferkel, F. Huisken, L. Holz, Y. N. Polivanov, V. V. Smirnov, O. M. Stelmakh, and R. Schmidt,” Deposition And Analysis of Silicon Clusters Generated By Laser-Induced Gas Phase Reaction,” J. Appl. Phys. 78, 5302, 1995

[1-16] T. S. Iwayama, S. Nakao, and K. Saitoh,” Visible Photoluminescence in Si^{+}-implanted Thermal Oxide Films on Crystalline Si,” Appl. Phys. Lett. 65, 1814, 1994

[1-17] G.A. Kachurin, S.G. Cherkova, V.A. Volodin, V.G. Kesler, A.K. Gutakovsky, A.G. Cherkov, A.V. Bublikov, and D.I. Tetelbaum,” Implantation of P Ions in SiO_2 Layers with Embedded Si Nanocrystals,” Phys. Res. B, 222(3-4), 497–504, 2004

[1-18] G. Belomoin, J. Therrien, A. Smith, S. Rao, and R. Twesten, S. Chaieb, M. H. Nayfeh, L. Wagner and L. Mitas," Observation of A Magic Discrete Family of Ultrabright Si Nanoparticles," Appl. Phys. Lett., 80, 841, 2002.

[1-19] A. Nakajima, Y. Sugita, K. Kawamura, H. Tomita, and N. Yokoyama,” Si Quantum Dot Formation with Low-Pressure Chemical Vapor Deposition,” Jpn. J. Appl. Phys., 35, L189, 1996

[1-20] F. Iacona, G. Franzò, and C. Spinella,” Correlation between Luminescence and Structural Properties of Si Nanocrystals,” J. Appl. Phys. 87, 1295, 2000

[1-21] A. A. Gonza´lez-Ferna´ndez, J. Juvert, Alfredo Morales-Sa´nchez, Jorge Barreto, M. Aceves-Mijares, and C. Dominguez,” Comparison of Electrical and Electro-Optical Characteristics of Light-Emitting Capacitors Based on Silicon-Rich Si-Oxide Fabricated By Plasma-Enhanced Chemical Vapor Deposition and Ion Implantation,” J. Appl. Phys. 111, 053109, 2002

[1-22] E. Werwa, A. A. Seraphin, L. A. Chiu, C. Zhou, and K. D. Kolenbrander,” Synthesis And Processing of Silicon Nanocrystallites Using A Pulsed Laser Ablation Supersonic Expansion Method,” Appl. Phys. Lett. 64, 1821, 1994

[1-23] E. Mota-Pineda, M. Meléndez-Lira, M. Zapata-Torres, P. del Angel, A. Pérez-Centeno, S. Jiménez-Sandoval, and M. A. Santana-Aranda,” Photoluminescence of As-Grown And Thermal Annealed SiO_x/Si-Nanocrystals Heterolayers Grown by Reactive RF Sputtering,” J. Appl. Phys. 108, 094323, 2010

[1-24] M. Zacharias, J. Heitmann, R. Scholz, U. Kahler, M. Schmidt, and J. Bl¨asing,

"Size-Controlled Highly Luminescent Silicon Nanocrystals: A SiO/SiO_2 Superlattice Approach," Appl. Phys. Lett., 80, 4, 661–663, 2002.

[1-25] L. L. Chang, L. Esaki, W. E. Howard, and R. Ludeke, "The Growth of A GaAs-GaAlAs Superlattice," J. Vac. Sci. Technol, 10, 1, 11–16, 1973.

[1-26] X. J. Hao, E. C.Cho, C. Flynn, Y. S. Shen, S. C. Park, G. Conibeer, and M. A. Green," Synthesis and Characterization of Boron-Doped Si Quantum Dots for All-Si Quantum Dot Tandem Solar Cells," Sol. Energy Mater. Sol. Cells, 93, 273-279, 2009

[1-27] X. J. Hao, E. C. Cho, G. Scardera, E. Bellet-Amalric, D. Bellet, Y. S. Shen, S. Huang, Y. D. Huang, G. Conibeer, and M. A. Green," Effects of Phosphorus Doping on Structural and Optical Properties of Silicon Nanocrystals in A SiO_2 Matrix," Thin Solid Films, 517, 5646, 2009

[1-28] X. J. Hao, E. C. Cho, G. Scardera, Y. S. Shen, E. Bellet-Amalric, D. Bellet, G. Conibeer, and M. A. Green," Phosphorus-Doped Silicon Quantum Dots for All-Silicon Quantum Dot Tandem Solar Cells," Sol. Energy Mater. Sol. Cells, 93, 1524, 2009

[1-29] S. Park , E. C. Cho, D. Song, G. Conibeer, M. A. Green, "N-Type Silicon Quantum Dots and P-Type Crystalline Silicon Heteroface Solar Cells." Sol. Energy Mater. Sol. Cells, 93, 684–690, 2009

[1-30] S. H. Hong, Y. S. Kim, W. Lee, Y. H. Kim, J. Y. Song, J. S. Jang, J. H. Park, S. H. Choi and K. J. Kim," Active Doping of B in Silicon Nanostructures and Development of A Si Quantum Dot Solar Cell," Nanotechnology, 22, 425203, 2011

[1-31] I. Perez-Wurf, X. Hao, A. Gentle, D. Kim, G. Conibeer, and M. A. Green," Si Nanocrystal p-i-n Diodes Fabricated on Quartz Substrates for Third Generation Solar Cell Applications," Appl. Phys. Lett., 95, 153506, 2009

Chapter 2 Fabrication of Gradient Si-Rich Oxide Multilayer (GSRO-ML) Structure for High Density Si QD Thin Film

In this chapter, we introduce the fabrication process of our samples. The process is shown in Fig. 2-1. In this study, we use two different substrates to analyze the characterization of GSRO thin films. One is Si (100) wafer for photoluminescence (PL) analysis, X-ray diffraction, transmission electron microscopy (TEM), and electrical measurements. The other one is quartz for Raman in order to avoid the crystalline Si signal from Si wafer at 520cm^{-1} in Raman spectra and for UV/Vis/NIR analysis.

Fig. 2-1 Fabrication process of GSRO thin films.

2.1 Substrate Clean

Before depositing thin films, the first step as shown in Fig. 2-1 is substrate clean. Si wafers are cleaned by standard RCA cleaning, and the standard process is shown in Fig. 2-2(a). The main purpose of RCA cleaning is to remove the particle, organic contaminates and native oxide on the wafer.

In the cleaning process of quartz, we clean quartz in acetone and ethanol for 10min by ultrasonic cleaner to remove organic contaminates on the quartz surface. The process is shown in Fig. 2-2(b).

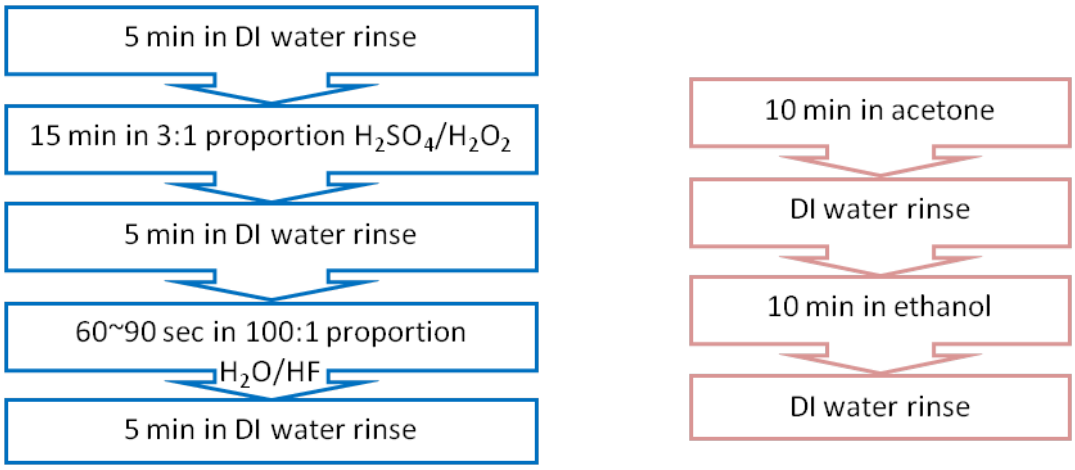

(a)

(b)

Fig. 2-2 Clean process chart of (a) Si wafer and (b) quartz substrates.

2.2 GSRO-ML Thin film Deposition

2.2.1 Principle of Radio Frequency (RF) Magnetron Sputtering Process

The basic principle of sputtering is to accelerate the ion to bombard the target surface, after ion and atomic in solid surface exchange the momentum, atoms will spill from the solid surface, this phenomenon called sputtering.

Sputtering mainly depend on the state of the plasma ions and free radicals. Plasma is also known as the fourth state of matter. Plasma's creation is similar to phase change in matter. By applying enough energy (like RF or microwave), gas can be broken down into plasma. In this state the plasma contains charged atoms, particles, ions and free radicals. Plasma is very chemically reactive due to its high energy state, making it very useful for changing the properties of material.

To ignite the plasma of the sputtering gas, cathode should be added to hundreds of volts. The bias added on cathode relative to the anode is negative, it shows when Ar atoms become Ar^+ ions, and they will be accelerated and impacted target, after collision, the atoms on the target surface flight and deposited on the substrate, that's the principle of sputtering (Fig. 2-3).

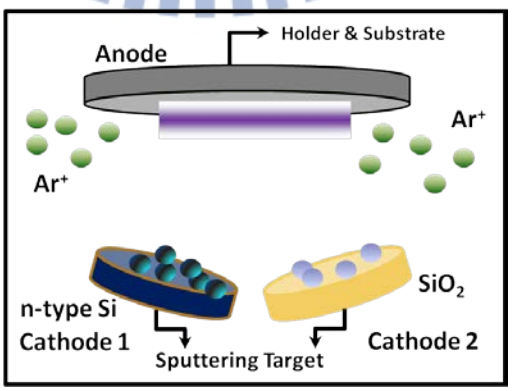

Fig. 2-3 Illustration of Operation of magnetron sputtering deposition method

2.2.2 GSRO-ML Thin Film

To deposit GSRO-ML thin films, co-sputtering by Si and SiO_2 targets are needed. During deposition, we fixed the power of SiO_2 in the low power, and tune the sputtering power of Si from 30 W to 110 W and to 30W by 1W/sec for 20 cycles, and the schematic diagram is shown in Fig. 2-4. By this method, we obtain a periodical gradient SRO distribution (Fig. 2-5).

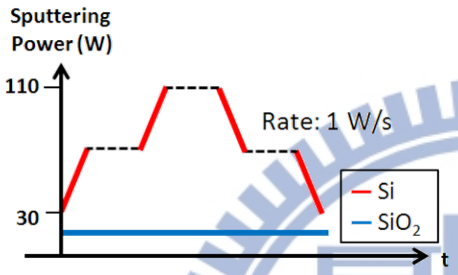

Fig. 2-4 The variation of Si concentration.

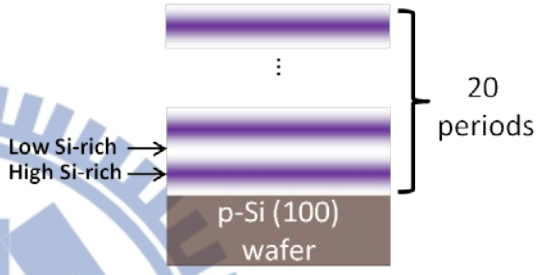

Fig. 2-5 Scheme of as-deposited GSRO-ML

2.3 Post-annealing Process

After deposition, the GSRO-ML thin films were treated with high temperature annealing process to precipitate Si atoms due to phase separation of Si and SiO_2 according to the following equation:

$$SiO_x \xrightarrow{\text{annealing}} \frac{x}{2}SiO_2 + \left(1 - \frac{x}{2}\right)Si \qquad (2\text{-}1)$$

Here we annealed all samples at 1100˚C for different durations in quartz furnace to form Si QD (Si QD).

Fig. 2-6 Scheme of as-deposited GSRO-ML structure.

2.4 Thermal Oxide Layer Remove

After annealing process, a thin thermal oxide layer was formed on the top and bottom of samples due to residual oxygen in the furnace. The thermal oxide layers make an influence on the collection efficiency of photo-generated carriers. In order to reduce the influence of the thermal oxide layers, we remove top side oxide layer by CHF_3:O_2 reactive ion etching (RIE) to and bottom oxide layers by buffered oxide etch (BOE).

2.5 Electrode Layer Deposition

Finally, contact electrodes were deposited on samples for the electrical properties measurement. We deposited Al layers on both top and bottom sides to form ohmic contact. The top electrodes are designed to square, as shown in Fig. 2-7. And another pattern which is for efficiency measurement is composed of a 5 mm*0.1 mm rectangle, the bar is a 0.2 mm* 4 mm rectangle, the pad is a 1.2 mm* 0.7 mm rectangle and the spacing is 0.29 mm (as shown in Fig. 2-7(b)).

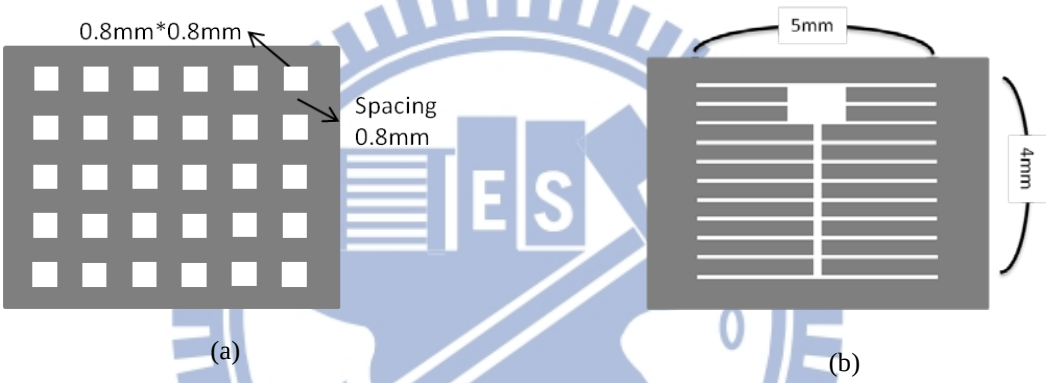

Fig. 2-7 Schemes of top electrodes of (a) square and (b) finger patterns deposited by thermal evaporation coater.

Chapter 3 Experimental Equipments and Analyzed Methods

In order to understand the characterization of the Si QD thin films. Some analyzed equipments are used, and the details are explained as below.

3.1 Raman Scattering Spectrum

Confocal-Raman microscope is a powerful characterization technique to study materials' vibration modes in a material. It's based on the Raman Effect [3-1], which is the inelastic scattering of photons and molecules when the incident photon interact with the molecules, the photons transit from the ground state to a virtual excited state. If the energy isn't absorbed by the molecules, it's released through the scattering method. Here shows the three different signal produced by the incident light interaction with the specimen in the Fig. 3-1. The released energy which is equal to the energy of the incident photons is called Raman scattering [3-1], and the incident light which interact with acoustic phonon is called Brilliouim scatter. Therefore, Raman microscope is a powerful and non-destructive technique to understand the materials' physical and chemical properties.

We analyzed the samples by high-resolution confocal Raman microscope (Lab RAM HR Raman Microscope), and used a 488-nm diode-pumped solid-state (DPSS) laser. The illuminated spot size is about 10um in diameter and the power of laser is about 7mW. Si substrate was used to calibrate the crystalline Si signal at 520 cm^{-1} before measuring our samples.

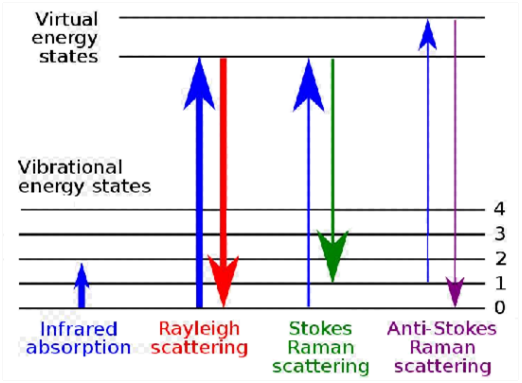

Fig. 3-1 Illustration of Rayleigh and Raman scattering

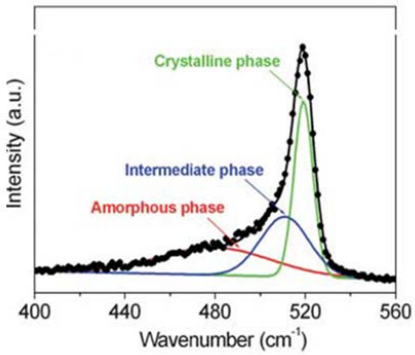

Fig. 3-2 Three components decomposed from Raman spectra of Si QD thin films[3-2]

Generally, three peaks can be detected in Si QD thin films, including amorphous phase (~480 cm^{-1}), intermediate phase (500 - 510 cm^{-1}) and crystalline phase (510 – 520 cm^{-1}) (Fig. 3-2) [3-2]. The crystallinity (χ_c) can be estimated by the following equation:

$$\chi_C = \frac{I_{nc}+I_i}{I_{nc}+I_i+I_a} \times 100\% \quad (3\text{- }1)$$

where I_{nc} is the intensity of crystalline phase, I_i and I_a represent the intensities of intermediate phase and amorphous mode, respectively.

In addition, peaks shift away from 520 cm^{-1} and the full width at half maximum (FWHM) of Raman spectra can be utilized to roughly estimate the dimension of Si NC because of the phonon confinement effect, as shown in Fig. 3-3 [3-3]. Phonon confinement mode can be expressed by the following equation:

$$L(w, D) \propto \int \frac{\sin[(qD/a)\pi]^2}{[1-(qD/a)^2]^2} \frac{dq}{[w_{opt}(q)-w]^2+(\Gamma/2)} \quad (3\text{- }2)$$

Where L(ω,D) is the lineshape of phonons confined to a hard sphere of diameter D, a is lattice parameter of Si, and Γ is the damping parameter [3-4].

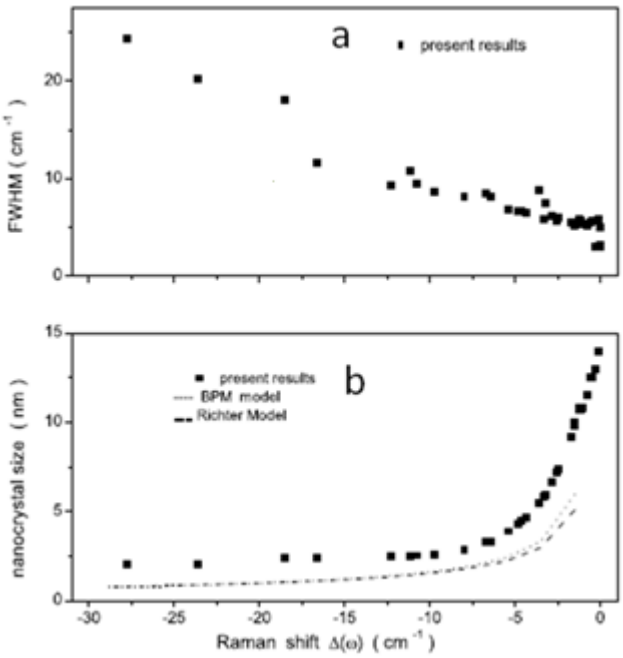

Fig. 3-3 FWHM of the Raman peaks and Si QD size against the corresponding Raman shift

3.4 Photoluminescence (PL) Spectrum

Photoluminescence (PL) spectroscopy is a contactless, nondestructive method of probing the electrical structure of materials. Light is incident directly onto samples where it's absorbed and imparts excess energy into the materials in a process called photo-excitation as shown in Fig. 3-4.

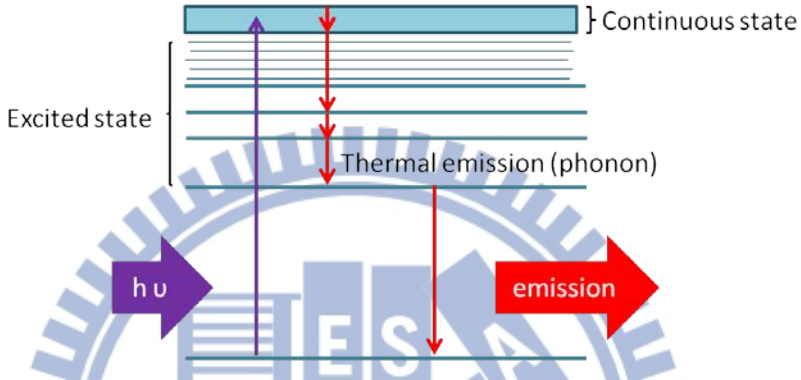

Fig. 3-4 Schematic of electronic transition.

The samples were analyzed by micro-PL measured on high-resolution Raman microscope (Lab RAM HR Raman Microscope). We used a laser on diode-pumped solid-state (DPSS) with a 488nm wavelength. The illuminated spot size is about 10um in diameter and the power of laser is about 7 mW. Si substrate is used to calibrate the laser signal at 488nm before PL spectroscopy measurement. All PL spectra were measured at room temperature (RT).

3.5 Ultraviolet/visible/Near-infrared (UV/VIS/NIR) Spectrum

In this section, we used UV/Vis/NIR spectrophotometer (Hitachi U-4100, Japan) to measure the transmittance (%T) and reflection (%R) of our thin films. We also can calculate the absorbance by

$$\text{Absorbance (\%)} = 100\text{-T-R (\%)} \quad (3\text{-}3)$$

Thus, we can understand the optical properties of the thin films. And, the absorption coefficient α can be got by the following relation

$$A\ (cm^{-1}) = A/t \quad (3\text{-}4)$$

where t is the thickness of thin films. The optical bandgap ($E_{g,opt}$) of the thin films are determined by the intercept of linear part of the absorption edge to αhν=0 in the relationship as [3-5]

$$(\alpha h\nu)^{\gamma} = B(h\nu - E_{g,opt}) \quad (3\text{-}5)$$

Where h is Plank's constant, ν is the frequency of the radiation, and B is the edge width parameter. The value of r is dependent on the $E_{g,opt}$ behavior, γ=1/2 for indirect $E_{g,opt}$ and γ=2 for direct $E_{g,opt}$.

3.6 Current-Voltage (I-V) Curve

The I-V curves in this study were measurement by the E5270B 8-slot precision measurement mainframe (Agilent Technologies) and a halogen lamp illumination with power density of 1 mW/cm^2 was applied to photo-response measurements. From the electrical properties, we can understand the rectification ratio, conductivity, and photo-responsive properties of our samples.

Reference

[3-1] C. V. Raman ,and K. S. Krishna, “A New Type of Secondary Radiation,” Nature, 121, 501, 1928

[3-2] Qijin Cheng; Tam, E.; Shuyan Xu; Ostrikov, K.," Si Quantum Dots Embedded in an Amorphous SiC Matrix: Nanophase Control by Non-Equilibrium Plasma Hydrogenation," Nanoscale, 594–600, 2010

[3-3] G. Faracil, S. Gibiliscol, P. Russol, A. R. Pennisil, G. Gompagnini, S. Battiato, R. Puglisi, and S. La Rosa “Si/SiO_2 Core Shell Clusters Probed by Raman Spectroscopy” Eur. Phys. J. B, 46, 457-461 ,2005

[3-4] S. Hernández, A. Martínez, P. Pellegrino, Y. Lebour, B. Garrido, E. Jordana, and J. M. Fedeli, “Silicon Nanocluster Crystallization in SiO_x Films Studied by Raman Scattering,” J. Appl. Phys., 104, 044304, 2008

[3-5] D. song, E. C. Cho, G. Conibeer, C. Flynn, Y. Huang, M. A. Green, “Structural Electrical And Photovoltaic Characterization of Si Nanocrystals Embedded SiC Matrix And Si Nanocrystals/C-Si Heterojunction Devices”, Sol. Energy Mater. Sol. Cells, 92, 474-480, 2008

Chapter 4 Results and Discussion

In this chapter, we discuss the GSRO-ML thin films with and without nucleation layer (NL), shown as Fig. 4-1. The Raman, PL, and UV/Vis/NIR spectra and TEM images and I-V curves are investigated for understanding the characteristics of the GSRO-ML thin films.

Fig. 4-1 Schemes of GSRO-ML thin films (a) without NL and (b) with NL

4.1 GSRO-ML Thin Films without NL

4.1.1 Crystalline Properties of GSRO-ML Thin Films without NL

So far, a GSRO-ML structure for the Si QD thin film hasn't been studied; hence, it's important to tune the deposition parameters for uniform QD's size and high QD's density formations. In the beginning, the gradient O/Si ratio is modified by tuning the SiO_2 sputtering power for the good NC-Si formation and suitable SRO composition. Table 4-1 shows the sputtering parameters of the GSRO-ML thin films without NL under different SiO_2 sputtering powers. The n-type Si sputtering power ($P_{n\text{-}Si}$) is periodically tuned from 30 to 110 and back to 30 W by rate of 1 W/sec while P_{SiO_2} is fixed at 10, 20, or 30 W for 20 periods (as shown in Fig. 2-4 and Fig. 2-5). Each GSRO thin layer thickness is about 2.5~3 nm. In order to understand

the NC-Si properties, the samples are annealed at 1100°C in N_2 ambient for 20 minutes after deposition.

To know the suitable parameters for the obvious NC-Si formation, the Raman spectra of the GSRO-ML thin films without NL under different P_{SiO2} are measured, as shown in Fig. 4-2. The signals can be decomposed into three components, including amorphous- (a-), intermediate- (i-Si), and nano-crystalline (NC-) Si phases, the curve-fitting results and the O/Si ratio form XPS measurements are listed in Table 4-2. The NC-Si intensities and crystallinity (C_{Si}) are obviously increased when the P_{SiO2} is decreased from 30 to 10 W, the results are well matched with the average O/Si ratio from XPS measurements. Hence, it indicates a low P_{SiO2} is necessary for the good NC-Si properties in a GSRO-Ml structure. To avoid the over-diffused Si-rich atoms during annealing, the P_{SiO2} of 20 W with medium O/Si ratio and obvious NC-Si intensity is used in the next experiments for preserving the QD's size control ability.

Table 4-1 Sputtering parameters of the GSRO-ML thin films without NL under different SiO_2 sputtering powers.

Sample ID	Sputtering power	
	$P_{n\text{-}Si}$ (W)	P_{SiO2} (W)
G30	Min.: 30 W Max.: 110 W Rate: 1 W/sec	30
G20		20
G10		10

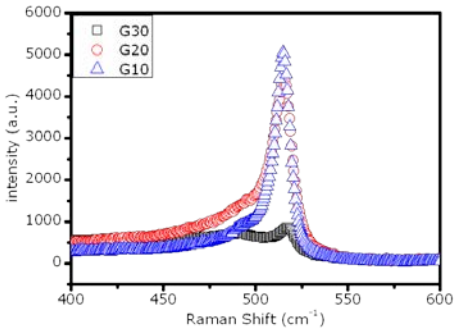

Fig. 4-2 Raman spectra of GSRO-ML thin films without NL under different SiO_2 sputtering powers.

Table 4-2 O/Si ratio from XPS measurements and the curve-fitting results from Fig. 4-2 for the NC-Si properties.

Sample ID	XPS	NC-Si properties after annealing from Raman spectrum			
	Ave. O/Si (%)	Peak Position (cm^{-1})	FWHM (cm^{-1})	C_{Si} (%)	Intensity (a.u.)
G30	0.84	517.4	10.0	42.5	8.6×10^3
G20	0.54	515.4	10.3	67.4	4.4×10^3
G10	0.39	515.0	8.8	82.3	5.1×10^3

4.2-1 GSRO-ML Thin Films with NL

In order to obtain the high density Si QD thin films with uniform QD's size, the NLs, which are co-sputtered by $P_{n\text{-}Si}$ of 110 W and P_{SiO_2} of 20 W for 1 nm thickness, are inserted into the GSRO-ML thin films in the centers of each GSRO thin-layer to enhance the localized Si-rich atoms aggregation ability during annealing, as shown in Fig. 4-3 and Fig. 4-4. The sputtering parameters of the GSRO-ML thin film with NL (Sample ID: G20-NL) are also listed in Table 4-3. Here a more suitable annealing duration time for a GSRO-ML structure is also studied for the Si QD thin films with better electro-optical properties. The Raman spectra of GSRO-ML with and without NL are shown in Fig. 4-5. The NC-Si intensity of G20-NL is increased by about two times compared with that of G20, it means the inserted NLs in GSRO-ML can efficiently enhance the NC-Si properties after annealing.

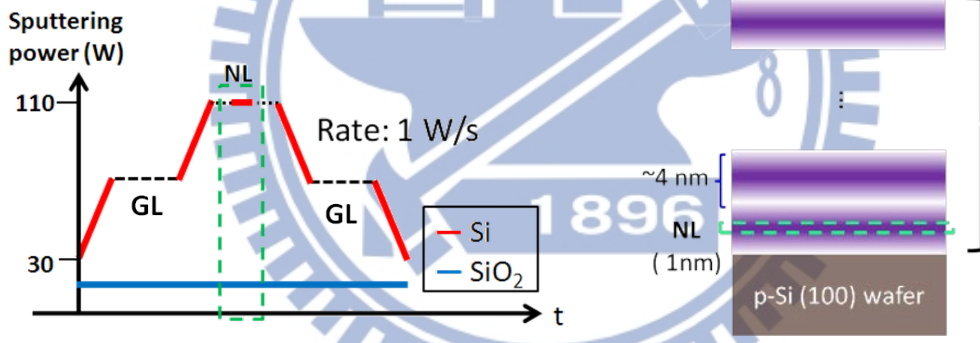

Fig. 4-3 Variations of Si and SiO_2 sputtering powers for each GSRO layer.

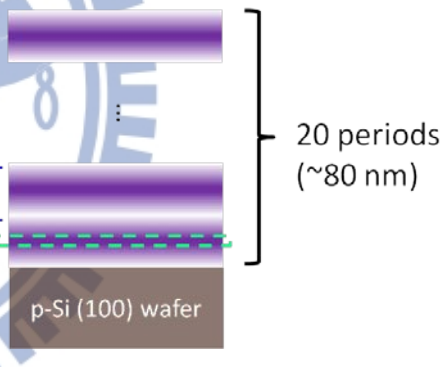

Fig. 4-4 Scheme of the GSRO-ML thin film with NL.

Table 4-3 Sputtering parameters of the GSRO-ML thin film with NL (Sample ID: G20-NL).

Sputtering power (W)			
Gradient layer (GL)		**Nucleation layer (NL)**	
$P_{n\text{-}Si}$ (W)	**P_{SiO2} (W)**	**$P_{n\text{-}Si}$ (W)**	**P_{SiO2} (W)**
Min.: 30W Max.: 110W Rate: 1 W/sec	20	110	20

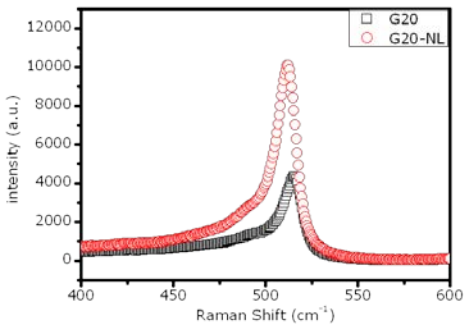

Fig. 4-5 Raman spectra of G20 and G20-NL.

4.2-1-1 Crystalline Properties of GSRO-ML Thin Films with NL

Fig. 4-6 shows the Raman spectra of G20-NL and the corresponding curve-fitting results under different annealing time are listed in Table 4-4. The higher C_{Si} and narrower FWHM are observed with increasing the annealing time; it means the larger average NC-Si QDs' size with better Si crystal quality is obtained by a longer annealing time.

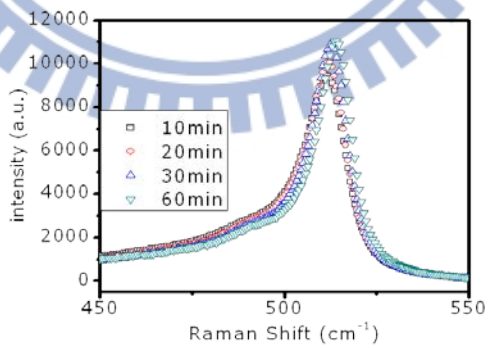

Fig. 4-6 Raman spectra of G20-NL under different annealing time.

Table 4-4 Curve-fitting results of Fig. 4-6 for the NC-Si properties.

Annealing time	Peak Position (cm^{-1})	FWHM (cm^{-1})	Intensity (a.u.)	C_{Si} (%)
10min	511.8	10.9	9.4×10^{3}	67.3
20min	512.1	10.4	1.0×10^{4}	72.3
30min	512.8	10.0	1.1×10^{4}	74.5
60min	514.0	9.8	1.1×10^{4}	75.4

4.2-1-2 Optical Properties of GSRO-ML Thin Films with NL

The absorption spectra in Tauc's plot for G20-NL under different annealing time are examined for the optical properties confirmations, as shown in Fig. 4-7, and the corresponding optical bandgap ($E_{g,opt}$) and the absorption coefficient (α) are also listed in Table 4-6. The $E_{g,opt}$ is increased by the longer annealing time due to a larger average Si QD size formation as observed in Table 4-5, besides, the α values of G20-NL annealed for 60 minutes is also significantly larger than that for 20minutes. The results represent that a longer annealing time can improve the optical absorption properties of the Si QD thin films in a GSRO-ML structure.

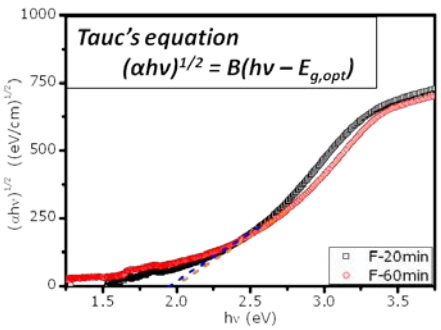

Fig. 4-7 Absorption spectra in Tauc's plot for G20-NL under different annealing time.

Table 4-6 Curve-fitting results for optical bandgap ($E_{g,opt}$) and absorption coefficient (α) from Fig. 4-7.

Annealing time	$E_{g,opt}$ (eV)	α (cm^{-1})
20min	2.02	2.2×10^3
60min	1.94	3.3×10^3

4.2-1-3 Electro-Optical Properties of GSRO-ML Thin Films with NL

To confirm the electro-optical properties of the GSRO-ML thin films under different annealing time, the I-V curves of G20-NL with and without a halogen lamp illumination about 1 mW/cm^2 of power density are shown in Fig. 4-8. The corresponding parameters are also listed in Table 4-7. G20-NL annealed for 60 minutes clearly shows not only a higher dark conductivity but also better photo-response properties, including V_{OC} and I_{SC} values, than that for 20 minutes. It may be contributed from the better Si crystal quality and optical absorption properties in the longer annealing time. Therefore, our results indicate that a long annealing time such as 60 minutes for the Si QD thin films using a GSRO-ML structure is more suitable for the better electro-optical properties.

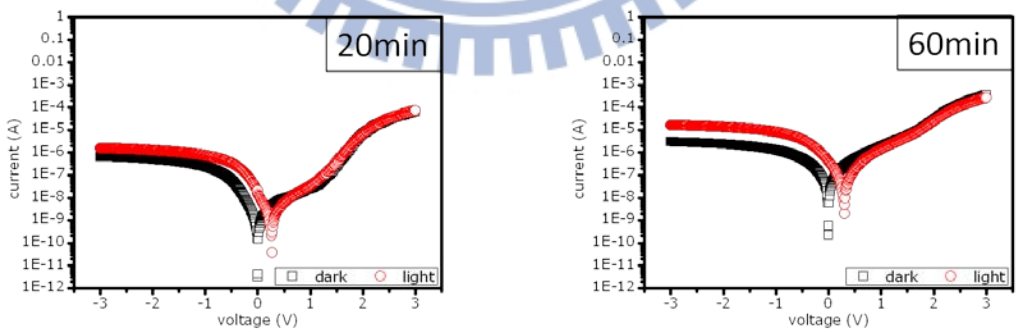

(a) (b)

Fig. 4-9 I-V curves of G20-NL on p-type Si(100) wafer with and without a halogen lamp illumination under an annealing duration time of (a) 20 and (b) 60 minutes.

Table 4-7 Parameters of the electro-optical properties of G20-NL under different annealing time. A halogen lamp with 1 mW/cm^2 of power density is used as the illumination source.

Annealing time	Conductivity $(\Omega\text{-cm})^{-1}$	V_{OC} (mV)	I_{SC} (A)
20min	2.4×10^{-7}	269	2.0×10^{-8}
60min	4.4×10^{-6}	298	4.2×10^{-7}

4.2-2 Comparison of Using GSRO-ML, [SRO/SiO_2]-ML, and SRO-SL Structures

In this section, the nano-structural and electro-optical properties of G20-NL using a GSRO-ML structure are compared to those of using [Si-rich oxide/SiO_2] multilayer ([SRO/SiO_2]-ML) and Si-rich oxide single layer (SRO-SL) structures, as shown in Fig. 4-4. The SRO-SL is deposited by co-sputtering n-Si target with $P_{n\text{-}Si}$ of 110 W and SiO_2 target with P_{SiO2} of 20 W for 80 nm of thickness equal to that of G20-NL. For [SRO/SiO_2]-ML, the SRO layers are deposited by co-sputtering n-Si target with $P_{n\text{-}Si}$ of 110 W and SiO_2 target with P_{SiO2} of 10 W, and each SRO and SiO_2 layer is individually fixed at 5 and 2.5 nm for 20 periods. All these samples are annealed at 1100°C for 60 minutes in N_2 ambient after deposition.

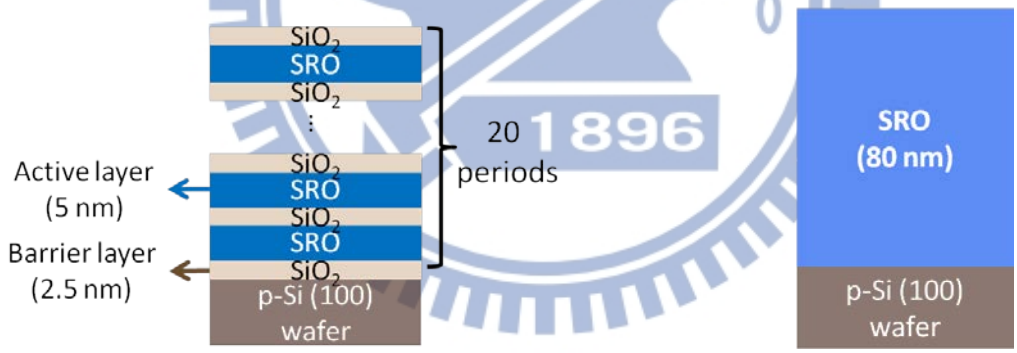

(a) (b)

Fig. 4-10 Schemes of (a) [SRO/SiO_2]-ML and (b) SRO-SL deposition structures

4.2-2-1 Crystalline Properties of GSRO-ML, [SRO/SiO_2]-ML, and SRO-SL Structures

The nano-crystalline properties of using three different structures are examined by Raman spectra, as shown in Fig. 4-11, and the corresponding curve-fitting results are listed in

Table 4-8. Among these three different structures, [SRO/SiO_2]-ML shows the lowest NC-Si intensity due to the highest average O/Si ratio than that of G20-NL or SRO-SL. However, G20-NL reveals the highest NC-Si intensity although it has a higher average O/Si ratio than SRO-SL. It represents using a GSRO-ML structure can enhance the Si-rich atoms aggregation to more efficiently form NC-Si during annealing. Besides, we notice that SRO-SL with a highly Si-rich oxide composition shows two peaks for c-Si phase not including the a- and i-Si phases. It means the size distribution of Si QDs formed during annealing is quite wide and the QD's size control ability is lost in a highly Si-rich SRO-SL structure. For [SRO/SiO_2]-ML and G20-NL, only one peak for nc-Si phase is obtained, hence, it represents that the good size control ability can be obtained by using both deposition structures. The close FWHM also means the similar average QD size in both samples, however, the C_{Si} of G20-NL is obviously higher than that of [SRO/SiO_2]-ML. Hence, compared to SRO-SL and [SRO/SiO_2]-ML, using a GSRO-ML structure has not only the NC-Si size control ability but also a better Si crystal quality.

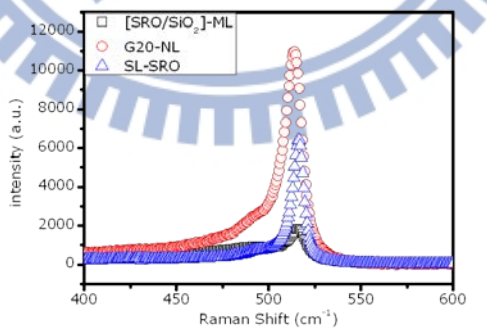

Fig. 4-11 Raman spectra of [SRO/SiO_2]-ML, G20-NL, and SRO-SL thin films.

Table 4-8 Curve-fitting results of Fig. 4-11.

Sample ID	NC-Si properties after annealing			
	Peak position (cm^{-1})	Peak FWHM (cm^{-1})	Intensity (a.u.)	Crystallinity (%)
[SRO/SiO_2]-ML	516.1	9.5	1.9×10^3	53.1
G20-NL	514.0	9.8	1.1×10^4	75.4
SRO-SL	513.9 516.5	11.2 5.9	6.4×10^3	97.3

4.2-2-2 Structural properties of GSRO-ML and [SRO/SiO_2]-ML Structures

To further understand the difference in the nano-structural properties between [SRO/SiO_2]-ML and G20-NL thin films, the high-resolution transmission electron microscope (TEM) images were examined by a JEOL JEM-2010F transmission electron microscope. Fig. 4-12 shows the cross-sectional high-resolution TEM images of the annealed [SRO/SiO_2]-ML and G20-NL ML thin films. From TEM images, the QD's size is similar but the QD's density of G20-NL is clearly higher than [SRO/SiO_2]-ML, this result is well matched with Raman spectra. In order to observe the size control abilities of both structures, we gather the QD's sizes from different regions shown in Fig. 4-13. The good size control ability can be observed in both samples since most QDs' sizes are located at 5±1 nm. However, the QD's density of G20-NL about 2.58×10^{12} cm^{-2} is significantly higher than [SRO/SiO_2]-ML about 1.04×10^{12} cm^{-2} by over 2 times. Therefore, the results demonstrate a GSRO-ML can also obviously increase the Si QD's density under preserving the Si QD size control ability.

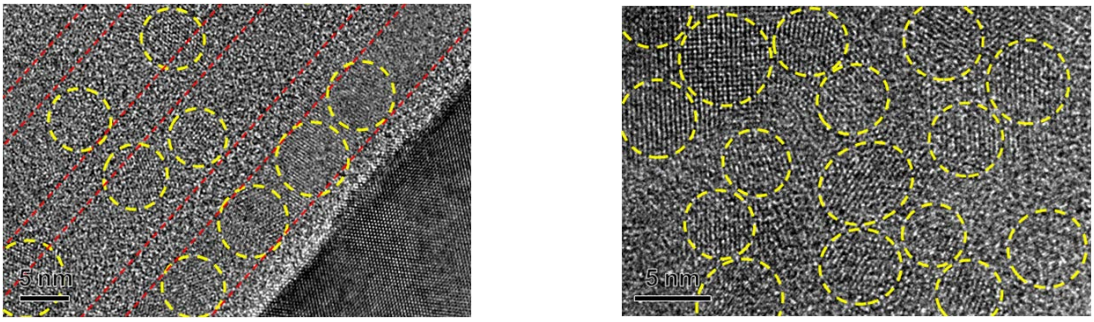

(a) (b)

Fig. 4-12 High-resolution TEM images of (a) [SRO/SiO_2]-ML and (b) G20-NL thin films.

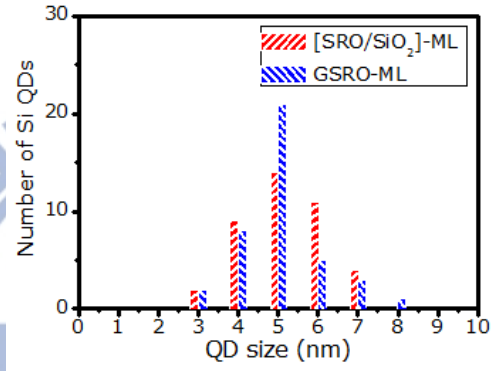

Fig. 4-13 QD's size distribution of [SRO/SiO_2]-ML and G20-NL thin films.

4.2-2-3 Optical Properties of GSRO-ML, [SRO/SiO_2]-ML, and SRO-SL Structures

In addition to crystalline properties, the optical properties are also investigated by PL and UV/Vis/NIR spectra. Fig. 4-14 shows the PL spectra of [SRO/SiO_2]-ML and G20-NL ML thin film. From literatures, the PL emission can be possibly contributed from three mechanisms, including interface states at the interfacial region between QDs and matrix [4-1, 4-2], quantum confinement (Q.C.) [4-3, 4-4] effect of Si QDs, and defect states inside SiO_2 matrix [4-5, 4-6]. The peak positions of the curve-fitting results from PL spectra are listed in Table 4-9. From Fig. 4-14, we observe that the emission intensity from Q. C. effect of G20-NL is lower than that of [SRO/SiO_2]-ML. In order to confirm the cause, the I-V curves of both samples under a 488

nm laser illumination are measured, as shown in Fig. 4-15, G20-NL shows more obvious photovoltaic properties than [SRO/SiO_2]-ML. It means that more photo-generated carriers can transport through QDs rather than recombine inside QDs due to the reduced QD's separation in G20-NL as observed in TEM images. On the other hand, the integrated intensity ratio of the emission from oxygen-related defect of G20-NL is higher than that of [SRO/SiO_2]-ML, it may be contributed from the all Si-rich oxide materials used in G20-NL. It's helpful for the PV properties of the Si QD thin films since the oxygen-related defects in SiO_2 matrix can enhance the carrier's transportation efficiency.

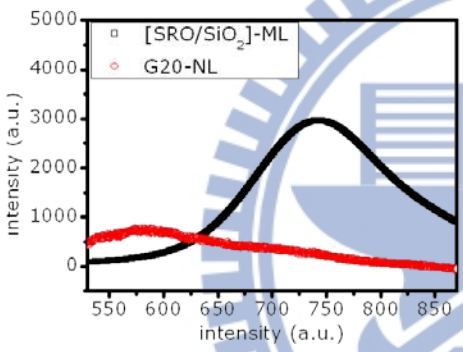

Fig. 4-14 PL spectra of [SRO/SiO_2]-ML and G20-NL.

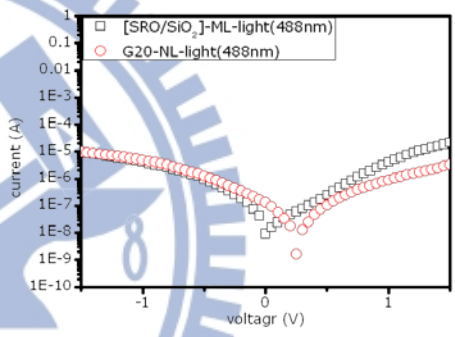

Fig. 4-15 I-V curves of [SRO/SiO_2]-ML and G20-NL under a 488 nm laser illumination.

Table 4-9 Curve-fitting results of Fig. 4-14.

Sample ID	Oxygen-related defect		Q.C. effect		Interfacial state	
	Position (nm)	Integrated intensity ratio (%)	Position (nm)	Integrated intensity ratio (%)	Position (nm)	Integrated intensity ratio (%)
[SRO/SiO_2]-ML	604	3.1	739 (1.68 eV)	83.3	849	13.6
G20-NL	577	62.3	705 (1.76 eV)	35.9	816	1.2

Fig. 4-16 shows the $(\alpha h\nu)^{1/2}$ versus $(h\nu)$ plots of [SRO/SiO_2]-ML and G20-NL, and the corresponding $E_{g,opt}$ and α values are listed in Table 4-10. The $E_{g,opt}$ value of G20-NL is slightly larger than that of [SRO/SiO_2]-ML matches with the results of the PL signals from Q. C. effect, which are peaks located at 1.68 eV for [SRO/SiO_2]-ML and 1.76 eV for G20-NL. It represents the effective E_g of G20-NL is surely higher than [SRO/SiO_2]-ML although both samples have the quite close distribution of QD's size. It may be originated from the difference in QD's surface structure or density. Besides, the α value of G20-NL is obviously higher than that of [SRO/SiO_2]-ML due to the higher QD's density obtained. It indicates a thinner film thickness is required for SC application integrating Si QD thin films by using a GSRO-ML structure.

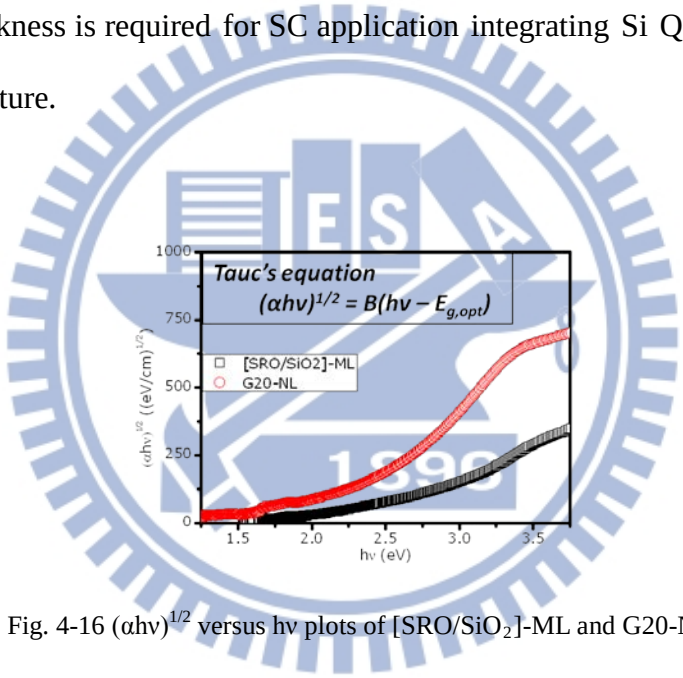

Fig. 4-16 $(\alpha h\nu)^{1/2}$ versus hν plots of [SRO/SiO_2]-ML and G20-NL thin films.

Table 4-10 Curve-fitting results of [SRO/SiO_2]-ML and G20-NL thin films.

Sample ID	$E_{g,opt}$ (eV)	α (cm^{-1})
[SRO/SiO_2]-ML	1.83	3.05×10^2
G20-NL	1.94	3.28×10^3

4.2-2-4 Electrical Properties

To understand the difference of the electro-optical properties of G20-NL and [SRO/SiO_2]-ML, the dark and light I-V curves are measured under a halogen lamp illumination with power density of ~1 mW/cm^2 as shown in Fig. 4-17. The corresponding parameters of electro-optical characteristic are listed in Table 4-11. Compared with [SRO/SiO_2]-ML, G20-NL shows the better photo-response behavior including the increased V_{OC} by 180 mV and I_{SC} by over ten times. As the previous results in TEM images, the improved photo-response properties in G20-NL can be attributed to the significantly higher QD's density, which also means the reduced QD's separation than that in [SRO/SiO_2]-ML.

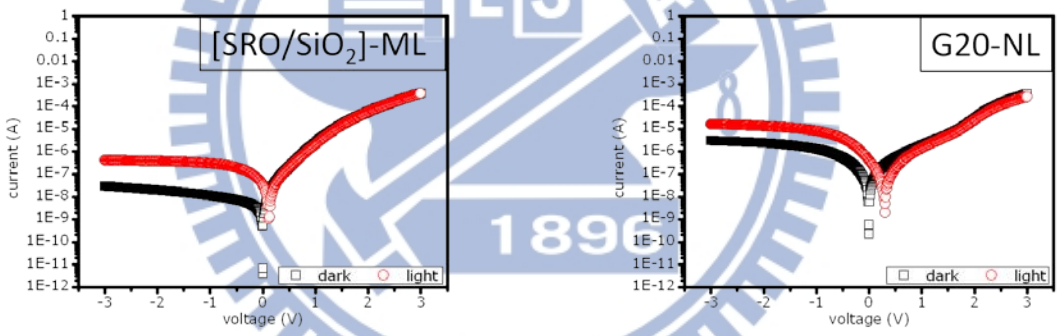

(a) (b)

Fig. 4-17 Dark and light I-V curves of (a) [SRO/SiO_2]-ML and (b) G20-NL on p-type Si wafers.

Table 4-11 Parameters of the photo-response properties of [SRO/SiO_2]-ML and G20-NL under a halogen lamp illumination

Sample ID	V_{OC} (mV)	I_{SC} (mA)
[SRO/SiO_2]-ML	118	3.5×10^{-8}
G20-NL	298	4.2×10^{-7}

4.2-2-5 Carrier's Transportation Mechanism of NC-Si QD Thin Film

The carrier's transportation mechanisms of G20-NL and [SRO/SiO_2]-ML thin films are studied here. The temperature-dependent ln(J/E) versus $E^{1/2}$ curves of both structures are performed, as shown in Fig. 4-18. The decreased curves' slopes under forward bias for [SRO/SiO_2]-ML are observed with increasing temperature but not in G20-NL. Hence, it indicates that the transportation mechanisms of both structures are surely different.

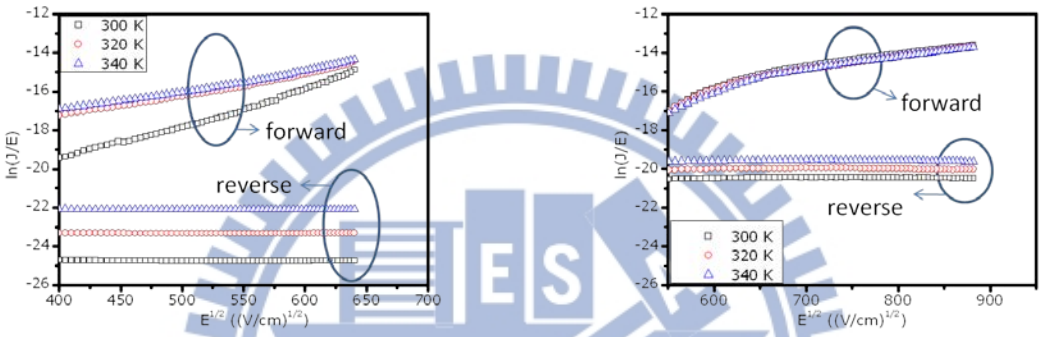

Fig. 4-18 Temperature-dependent current versus voltage (I–V–T) characteristics of (a) [SRO/SiO_2]-ML and (b) G20-NL-ML thin film structure measured in the temperature range 300–340K using 20K steps.

In order to further confirm the carrier's transportation mechanism, the I-V curve of G20-NL under forward bias in log-to-log plot is shown in Fig. 4-19(a); it can be described by two-diode model expressed as [4-7]

$$J(V) = J_{01}\left(\exp\left(\frac{V-IR_s}{n_1 kT/q}\right)-1\right) + J_{02}\left(\exp\left(\frac{V-IR_s}{n_2 kT/q}\right)-1\right) + \frac{(V-IR_s)}{R_{sh}} \qquad (4\text{-}1)$$

where q is the electron charge, k is the Boltzmann constant, T is the absolute temperature, n_1 and n_2 are the diode ideality factor, R_s and R_{sh} are series and shunt resistor, J_{01} and J_{02} are the saturation current densities for the two-diode. Here shows three regions labeled region I, II, and III in Fig. 4-19(a). In region I, the current increased linearly with the low bias (V<0.5 V). This indicates the presence of a parallel current path due to a shunt resistor R_{sh} in parallel to

the junction which is responsible for these currents. The diode current is given by Ohm's law I = V/R_{sh}. In region II, the current increased exponentially with the larger bias (0.5 V< V< 2.5 V) applied, indicated that a different transportation mechanism dominants. The relationship between current and bias can be described by a standard diode equation expressed as

$$J(V,T) = J_0(T)[\exp(AV) - 1] \quad \text{where } J_0 \propto \exp\left(-\frac{E_a}{kT}\right) \tag{4-2}$$

The carrier's transportation mechanisms are shown in Table 4-12 [4-8]. In region III, larger bias applied (V> 2.5 V), the current increased more slowly and deviates from exponential behavior. In space-charge limited current (SCLC) model, the current and bias can be described by

$$J = KV^M \tag{4-3}$$

where K is a function of the thickness and trap distribution and M depends on the density of states in the Si QD thin films.

However, [SRO/SiO_2]-ML can't be described by two-diode model mentioned above. Another model proposed by V. Osinniy et al. in 2009 combining the direct and phonon-assisted tunneling mechanisms [4-8]. The J-E curve of [SRO/SiO_2]-ML in log-to-log plot shown in Fig. 4-19 (b), it shows the linear relationship with two slopes. In the high electrical field region ($E > 10^5$ V/cm), the transportation mechanism is dominated by Poole-Frenkel emission model [4-9, 4-10, 4- 11]. The current density (J_{PF}) in this model is given by:

$$J_{PF} = CE\exp\left[-\frac{q\psi}{nk_BT} + (q^3E/\pi\varepsilon)^{1/2}/nk_BT\right] \tag{4-4}$$

where *C*, *E*, Ψ, n, ε, and *T* are a system-specific constant, the electric field, the escape barrier height for electrons from traps, a factor which varies between one and two depending on the amount of acceptor/donor compensation, the dielectric constant of the SiO_2 layer, and the temperature, respectively. In the low electrical field region, there exists another transportation mechanism described by direct tunneling made in the frame of the Wentzel–Kramers–Brillouin (WKB) approximation of barrier transparency [4-12, 4-13] expressed as

$$J_{DT}=J_0\left(1-\frac{V_{ox}}{2\Phi_B}\right)\exp\left\{-\frac{4}{3}\frac{\sqrt{2m^*q}}{\hbar}\frac{t_{ox}\Phi_B^{3/2}}{V_{ox}}\times\left[1-\left(1-\frac{V_{ox}}{\Phi_B}\right)^{3/2}\right]\right\} \quad (4\text{- }5)$$

where J_0, V_{ox}, Φ_B and t_{ox} are the voltage-independent constants that is governed by the oxide thickness and barrier height, the voltage drop across the dielectric medium, the conduction band potential barrier for the direct tunneling and the dielectric thickness, respectively. Therefore, the transportation mechanisms of both structures have been demonstrated, it's dominated by two-diode model for G20-NL and direct and phonon-assisted tunneling method for [SRO/SiO_2]-ML. And the large enhancement of electro-optical properties for G20-NL compared to [SRO/SiO_2]-ML can be attributed to the different carrier transport mechanism.

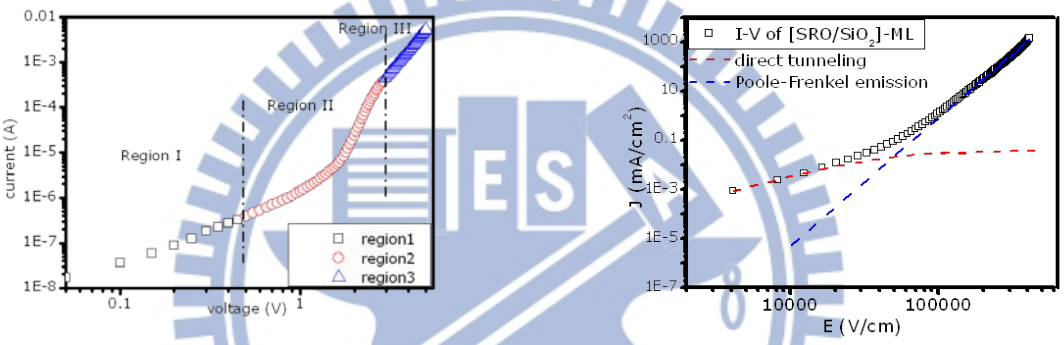

(a) (b)

Fig. 4-19 (a) I-V curve of G20-NL and (b) J-E curve of [SRO/SiO_2]-ML.

Table 4-12 Four different carrier's transportation mechanisms through a junction [4-7].

Mechanism	**J_0**	**A**	**n**
Diffusion	$J_0 \propto \exp(-E_g/kT)$	A=q/kT	n=1
Recombination	$J_0 \propto \exp(-E_g/2kT)$	A=q/nkT	$n \leqq 2$
Tunneling	$J_0 \propto \exp(-E_g/kT)$	A=constant	n≠constant
Thermionic	$J_0 \propto \exp(-\Phi_g/kT)$	A=q/kT	n=1

4.3 GSRO-ML Thin Films with Highly Doping NL

In order to improve the electro-optical properties of Si QD thin films, some groups had largely increased the doping concentration for better PV performance. Here we increase the P-doping concentration in the NLs of the GSRO-ML thin films for further enhancing the electro-optical properties of the Si QD thin films. We deposited the generally (N_P~1×10^{18} cm^{-3}; G20-NL(n-Si)) and highly (N_P~1×10^{19} cm^{-3}; Sample ID: G20-NL(n^+-Si)) P-doping Si layers as NLs shown in Fig. 4-20. After deposition, both samples are also annealed at 1100°C for 60 minutes in N_2 ambient for Si QDs formation.

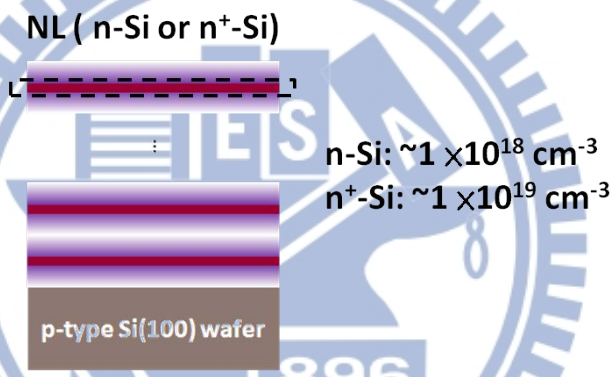

Fig. 4-20 Scheme of GSRO-ML with different P-doping concentration.

4.3.1 Electrical Properties of GSRO-ML Thin Films with Highly Doping NL

The dark and light I-V curves of G20-NL(n-Si) and G20-NL(n^+-Si) are measured shown in Fig. 4-21, and the corresponding parameters of the electro-optical characteristics are listed in Table 4-13. The dark conductivity and photo-response properties of G20-NL(n^+-Si) are obviously higher than those of G20-NL(n-Si), hence, it means that a higher P-doping concentration in a GSRO-ML structure can efficiently enhance the electro-optical characteristics of the Si QD thin films.

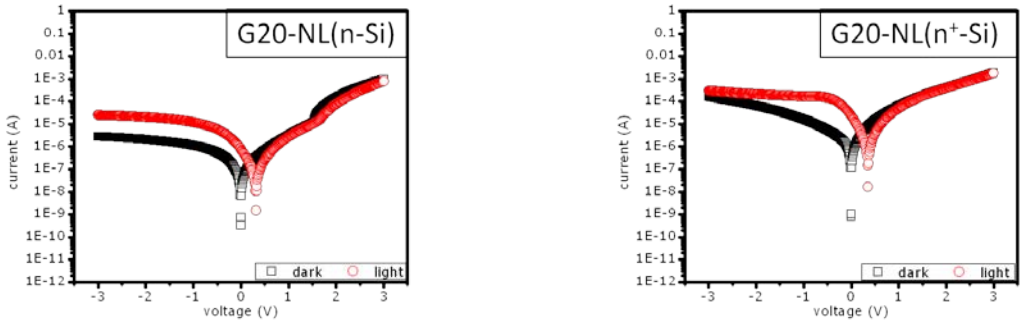

(a) (b)

Fig. 4-21 Dark and light I-V curves of (a) G20-NL(n-Si) and (b) G20-NL(n^+-Si).

Table 4-13 Parameters of the electro-optical characteristics for G20-NL(n-Si) and G20-NL(n^+-Si) under a halogen lamp illumination.

Sample ID	Vertical conductivity $(\Omega\text{-cm})^{-1}$	V_{OC} (mV)	I_{SC} (mA)
G20-NL(n-Si)	4.4×10^{-6}	320	7.9×10^{-7}
G20-NL(n^+-Si)	2.1×10^{-5}	360	2.4×10^{-5}

4.3.2 H_2 Passivation Effect

Though, the electrical properties can be improved by increasing the doping concentration, the further improvement on fill factor (F.F.) is still needed for further PV properties enhancements. Hence, we use a low-temperature post-annealing process in a forming gas (N_2:H_2=95:5) ambient from 300 ~ 500˚C after 1100˚C annealing to passivate the dangling bonds or interface states at the QDs' surface[4-1, 4-5, 4-14].

The dark and light I-V curves of G20-NL(n^+-Si) annealed in N_2+H_2 under different post-annealing temperature are shown in Fig. 4-22, and the corresponding parameters of photo-response properties are listed in Table 4-14. The series resistances (R_s) of the samples (as fabricated, 300˚C, 400˚C, and 500˚C) from the light I-V curves are also listed in Table 4-15. It's

observed that the R_s values are obviously decreasing with increasing the annealing temperature. The dark I-V curves are improved by increasing the annealing temperature in the forming gas, however, the optimal photo-response properties including the V_{OC}, I_{SC}, and F.F. values are observed in the sample annealed at 400˚C in the forming gas. It may be resulted from the difficulty on efficiently forming the Si-H or Si-OH bonds to passivate the dangling bonds or interface states at the QDs' surface in these annealing temperatures of 300 and 500˚C.[4-1, 4-5, 4-14]

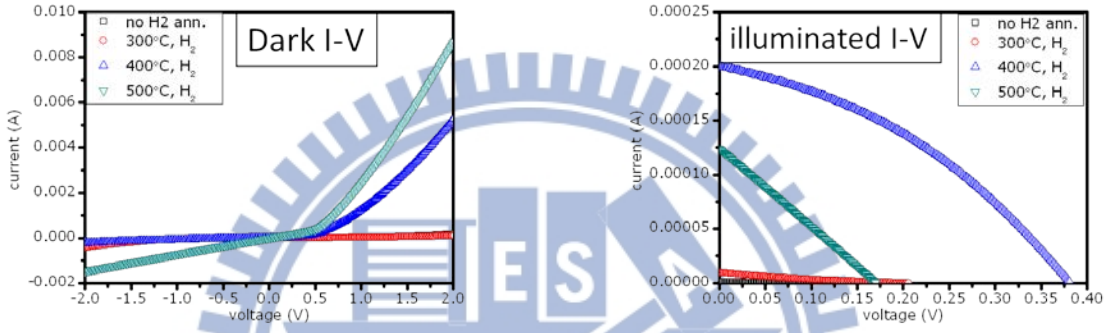

(a) (b)

Fig. 4-22 (a) Dark and (b) light I-V curves of G20-NL(n^+-Si) annealed in forming gas under different post-annealing temperature.

Table 4-14 Parameters of the electro-optical characteristics of G20-NL(n^+-Si) annealed in forming gas under different post-annealing temperature from Fig. 4-23.

	V_{OC} (mV)	I_{SC} (A)	F.F. (%)
No H_2 ann.	118	1.3×10^{-6}	22.9
300˚C, H_2	220	6.5×10^{-6}	22.3
400˚C, H_2	380	2.1×10^{-4}	36.9
500˚C, H_2	160	1.2×10^{-4}	25.4

Table 4-15 Parameters of the series resistances (R_s) from Fig. 4-24(b).

	No H_2 ann.	300˚C	400˚C	500˚C
R_s (Ω)	1.0×10^5	2.2×10^4	1.1×10^3	1.2×10^3

To further confirm the hydrogen passivation effect, the electro-optical properties of the sample annealed at 400°C in forming gas is compared with that in pure N_2 ambient, as shown in Fig. 4-25. The corresponding parameters are listed in Table 4-16. The sample annealed in pure N_2 ambient is also improved in electro-optical properties. However, the conductivity in the forward-bias region is lower and the leakage current in the reverse-bias region is larger than the sample annealed in forming gas. Besides, the V_{OC}, I_{SC} and F.F. of the sample annealed in pure N_2 ambient are lower than those annealed in forming gas. To understand the difference between annealing in pure N_2 and forming gas, the values of series resistances extracted from the light I-V curves are listed in

Table 4-17. We can observe that the series resistance of sample annealed in pure N_2 is smaller than that in forming gas, it may result from the larger leakage current and worse photo-response properties. It can be concluded that annealing in pure N_2 ambient can passivate defect states [4-15] but the ability of passivation of N atoms is not as good as H atoms.

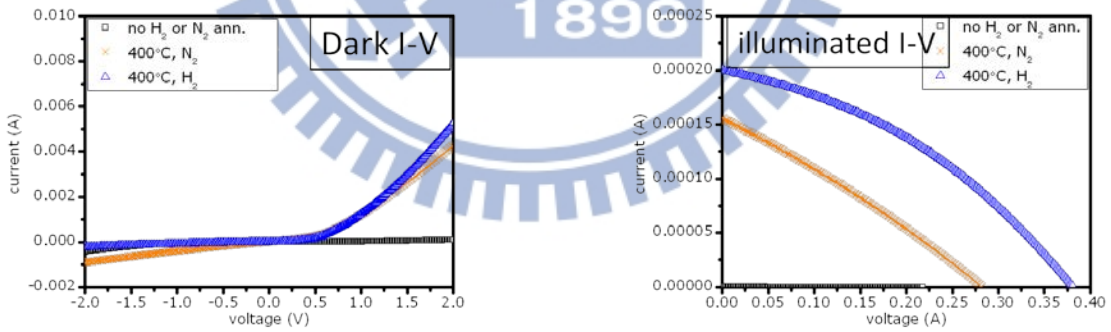

(a) (b)

Fig. 4-25 (a) Dark and (b) light I-V curves of G20-NL (n^+-Si) annealed at 400°C for 1 hour in N_2 or N_2+H_2.

Table 4-16 Parameters of the electro-optical characteristics of G20-NL (n^+-Si) from Fig. 4-26(b).

	V_{OC} (mV)	I_{SC} (A)	F.F.(%)
No H_2 or N_2 ann.	118	1.3×10^{-6}	22.9
400°C, N_2	300	1.6×10^{-4}	28.2
400°C,(N_2+H_2)	380	2.1×10^{-4}	36.9

Table 4-17 Parameters of the series resistances (R_s) extracted from Fig. 4-27(b).

	no H_2 or N_2 ann.	400°C, N_2	400°C,(N2+ H_2)
R_s (Ω)	1.0×10^5	1.3×10^3	1.1×10^3

Reference

[4-1] M. V. Wolkin, J. Jorne, P. M. Fauchet, G. Allan, and C. Delerue, “Electronic states and luminescence in porous silicon quantum dots: The role of oxygen,” Phys. Rev. Lett., vol. 82, pp. 197-200, 1999.

[4-2] Daniel Hiller, Mihaela Jivanescu, Andre Stesmans, and Margit Zacharias," Pb(0) centers at the Si-nanocrystal/SiO2 interface as the dominant photoluminescence quenching defect," J. Appl. Phys. 107, 084309, 2010

[4-3] Y. Kanemitsu, T. Ogawa, K. Shiraishi, and K. Takeda, “Visible PL from oxidized Si nanometer-sized spheres: Exciton confinement on a spherical shell,” Phys. Rev. B, vol. 48, pp. 4883- 4886, 1993.

[4-4] S. Schuppler, S. L. Friedman, M. A. Marcus, D. L. Adler, and Y.-H. Xie, “Size, shape, and composition of luminescent species in oxidized Si nanocrystals and H-passivated porous Si,” Phys. Rev. B, vol. 52, pp. 4910- 4925, 1995.

[4-5] J. S. Biteen, N. S. Lewis, H. A. Atwater, and A. Polman," Size-dependent oxygen-related electronic states in silicon nanocrystals," Appl. Phys. Lett., 84, 5389, 2004

[4-6] X. X. Wang, J. G. Zhang, L. Ding, B. W. Cheng, W. K. Ge, J. Z. Yu, and Q. M. Wang, “Origin and evolution of photoluminescence from Si nanocrystals embedded in a SiO_2 matrix,” Phys. Rev. B 72, 195313, 2005

[4-7] L. F. Marsal, J. Pallares, X. Correig, A. Orpella, D. Bardés, R. Alcubilla,” Analysis of Conduction Mechanisms in Annealed N-$Si_{1-x}c_x$:H/P-Crystalline Si Heterojunction Diodes for Different Doping Concentrations,” J. Appl. Phys., 85, 1216, 1999

[4-8] V. Osinniy, S. Lysgaard, V. l. Kolkovsky, V. Pankratov, and A. Nylandsted Larsen," Vertical Charge-Carrier Transport in Si Nanocrystal/SiO_2 Multilayer Structures," Nanotechnology, 20, 195201, 2009

[4-9] J. Frenkel," On Pre-Breakdown Phenomena in Insulators and Electronic Semi-Conductors," Phys. Rev. 54, 647–648, 1938

[4-10] P. Blood and J. W. Orton," The Electrical Characterization of Semiconductors: Major Carriers and Electron States," London: Academic, 1992

[4- 11] W. R. Harell and J. Frey," Observation of Poole–Frenkel Effect Saturation in SiO_2 and Other Insulating Films," Thin Solid Films, 352, 195-204, 1999

[4-12] T. Ando,A.B. Fowler and F. Stern," Electronic Properties of Two-Dimensional Systems," Rev. Mod. Phys., 54, 437, 1982

[4-13] H. Wong and H. Iwai," Modeling and Characterization of Direct-Tunneling Current

in Dual-Layer Ultrathin-Gate Dielectric Films," J. Vac. Sci. Technol. B, 24, 1785, 2006
[4-14] A. R. Wilkinson and R. G. Elliman,” Kinetics of H_2 Passivation of Si Nanocrystals in SiO_2,” Phys. Rev. B, 68, 155302, 2003
[4-15] M. S. Yang, K. S. Cho, J. H. Jhe, S. Y. Seo, J. H. Shin, K. J. Kim and D. W. Moon," Effect of Nitride Passivation on The Visible Photoluminescence From Si-Nanocrystals," Appl. Phys. Lett., 85, 16, 2004

Chapter 5 Conclusion and Future Work

5.1 Conclusion

In this study, the high density Si QD thin film with good QD size controlling ability and small QD separation have been successfully developed by a GSRO-ML deposition structure and suitable annealing condition. Firstly, we focus on tuning the sputtering powers of n-type Si and SiO_2 targets to obtain a suitably average O/Si ratio. In order to enhance the nano-structural properties, the ultra thin (~1 nm) and highly Si-rich SRO layers are inserted into each GRSO layer as NL. The G20-NL shows the higher absorption coefficient and the better electro-optical characteristic than that of [SRO/SiO_2]-ML structure. TEM images show that higher density of Si QD in G20-NL than that in [SRO/SiO_2]-ML thin film. It's suspected that the reduced spacing of QDs due to the enhanced QD density improve the carrier transportation property and result in the obvious enhancements in the electro-optical properties. In the third part, we introduce the highly P-doped (~$1x10^{19}$ cm^{-3}) Si QD thin film as NL to enhance the conductivity of GSRO thin film. The conductivity and I_{SC} are enhanced by ~5 times and 2 orders of magnitude, respectively. After annealing at 400°C in N_2(95%)+H_2(5%) gas for 1 hour, the I_{SC} enhanced by ~25 times and the F.F. increased over 2 times are observed. It proved that the treatment of H_2 annealing can reduce the series resistor effectively, and the I_{SC} and F.F. can be enhanced. A higher conversion efficiency of Si QD thin films utilizing a GSRO-ML structure with heavy doped concentration can be deeply expected in the near future.

5.2 Future Work

5.2.1 Heavy Doping Si QD Thin Film

Based on the results of reference [5- 1], Fig. 5- 1 shows the photo-response properties vary with different B-doping concentration. As B-doping concentration (n_B) increases from 6.0×10^{19} to 1.0×10^{21} cm^{-3}, V_{OC} gradually increases, while J_{SC} shows a maximum at about $n_B=6.3\times10^{20}$ cm^{-3}. As shown in the inset of Fig. 5- 1, other photovoltaic parameters such as fill factor and energy-conversion efficiency also show doping-dependent behaviors similar to that of J_{SC}. The decrease of the three photovoltaic parameters above $n_B=6.3\times10^{20}$ atoms/cm^3 is thought to be related to the increased defect density. Hence, it can be deeply expect that a higher efficiency will be obtained by GSRO-ML structures with higher doping concentration.

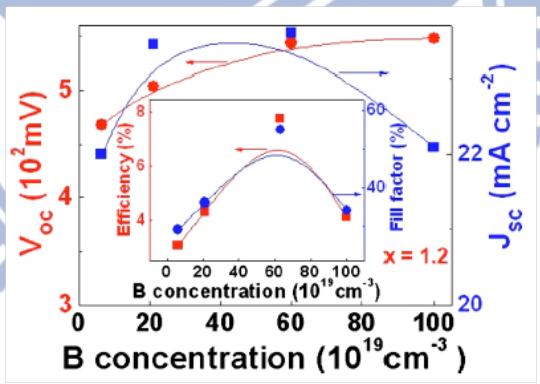

Fig. 5- 1 V_{OC} and J_{SC} as functions of B-doping concentration (n_B). The inset shows fill factor and energy-conversion efficiency as functions of n_B [5- 1].

5.2.2 High Efficiency p-i-n Si QD Thin Film SCs

Finally, to achieve p-i-n tandem cells, the undoped and p-type thin films are needed. Therefore, we also begin to investigate undoped and P-type GSRO thin films. Fig. 5-2 shows the comparison of p-type [SRO/SiO_2]-ML and GSRO-ML (with general doping-concentration

NL and the thickness is 5 A) thin films. Though several conditions, such as NL's thickness, doping concentration and annealing time, are not optimization, the enhancements on electro-optical properties can be observed.

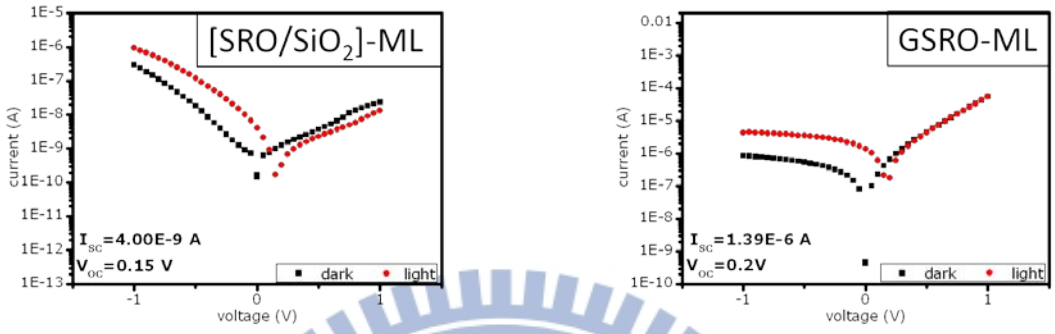

Fig. 5-2 I-V curves of p-type (a) [SRO/SiO_2]-ML and (b) GSRO-ML thin films on Si wafer under a halogen lamp illumination.

Reference

[5- 1] S. H. Hong, J. H. Park, D. H. Shin, C. O. Kim, S. H. Choi, and K. J. Kim, "Doping- and Size-Dependent Photovoltaic Properties of P-Type Si-Quantum Dot Heterojunction Solar Cells: Correlation with Photoluminescence," Appl. Phys. Lett., 97, 072108, 2010